Temporal and Spatial Characteristics of AIRS and CERES OLR Climatologies and Anomaly Time Series

Joel Susskind[1], Jae Lee[2], Lena Iredell[3], and Norman G. Loeb[4]

[1]NASA GSFC
[2]University of Maryland
[3]SAIC @ NASA GSFC
[4]NASA Langley Research Center

November 24, 2022

Abstract

This paper compares the characteristics of the monthly mean AIRS Version-6 and CERES_EBAF Edition 4.0 OLR data sets over a 14-year overlap period, September 2002 through August 2016. These comparisons include spatial plots of monthly mean OLR climatologies and spatial plots of OLR Average Rates of Change (ARCs), representative of the slopes of the linear least squares fits to anomaly time series. This paper also compares spatial plots of El Niño Correlations (ENCs) of the AIRS OLR and CERES OLR anomaly time series. ENCs represent temporal correlations of anomaly time series with an El Niño Index that we define in this paper. In addition, we show ARCs and ENCs of select derived AIRS geophysical parameters that help explain OLR variability in space and time. There are separate AIRS data sets that use data observed only in ascending Aqua orbits (AIRS) and data observed only in descending Aqua orbits (AIRS). An additional data set of AIRS products exists based on observations made in both orbits (AIRS). There is excellent agreement between the ARCs of CERES OLR and the ARCs of AIRS OLR down to the 1@ by 1@ longitude spatial scale. The AIRS OLR product displays a positive global mean monthly mean bias compared to CERES OLR of roughly 3.0 W/m that is essentially constant in space and time. The largest differences between AIRS OLR and CERES OLR monthly climatologies and anomaly time series occur in regions where the diurnal differences of AIRS OLR are largest.

1   Temporal and Spatial Characteristics of AIRS and CERES OLR Climatologies and
2   Anomaly Time Series

3

4   Joel Susskind, NASA Goddard Space Flight Center

5 Jae N. Lee, Joint Center for Earth Systems Technology, University of Maryland,
6   Baltimore County

7   Lena Iredell, ADNET

8   Norman G. Loeb, NASA Langley Research Center

9

10

11

12

13 Key Points

14

15 This paper compares the temporal and spatial characteristics of the monthly mean
16 AIRS Version-6 OLR and CERES EBAF_Edition 4.0 OLR data sets over the period
17 2003 through 2016.

18 AIRS OLR displays a positive global mean bias as compared to CERES OLR of
19 approximately 3.0 W/m^2 that is essentially constant in space and time.

20 There is excellent agreement between the spatial distributions of monthly mean
21 AIRS and CERES OLR climatologies, as well as of the trends of the AIRS and CERES
22 OLR anomaly time series and their correlations with an El Niño Index. The largest
23 AIRS/CERES OLR differences occur in places where diurnal differences of AIRS OLR
24 are largest.

25 This agreement also validates the AIRS retrieved geophysical parameters. These
26 geophysical parameters help explain the factors influencing OLR variability.

27

28

29

30

31   Abstract

32   This paper compares the characteristics of the monthly mean AIRS Version-6 and

33   CERES_EBAF Edition 4.0 OLR data sets over a 14-year overlap period, September

34   2002 through August 2016. These comparisons include spatial plots of monthly

35   mean OLR climatologies and spatial plots of OLR Average Rates of Change (ARCs),

36   representative of the slopes of the linear least squares fits to anomaly time series.

37   This paper also compares spatial plots of El Niño Correlations (ENCs) of the AIRS

38   OLR and CERES OLR anomaly time series. ENCs represent temporal correlations of

39   anomaly time series with an El Niño Index that we define in this paper. In addition,

40   we show ARCs and ENCs of select derived AIRS geophysical parameters that help

41   explain OLR variability in space and time.

42   AIRS flies on EOS Aqua. There are separate AIRS data sets that use data observed

43   only in ascending Aqua orbits (AIRS$_{PM}$) and data observed only in descending Aqua

44   orbits (AIRS$_{AM}$). An additional data set of AIRS products exists based on

45   observations made in both orbits (AIRS$_{AVG}$). There is excellent agreement between

46   the ARCs of CERES OLR and the ARCs of AIRS$_{AVG}$ OLR down to the 1˚ latitude by 1˚

47   longitude spatial scale.   The AIRS$_{AVG}$ OLR product displays a positive global mean

48   monthly mean bias compared to CERES OLR of roughly 3.0 W/m^2 that is essentially

49   constant in space and time. The largest differences between AIRS$_{AVG}$ OLR and

50   CERES OLR monthly climatologies and anomaly time series occur in regions where

51   the diurnal differences of AIRS OLR are largest.

1

52   AIRS OLR and CERES OLR are independent products. The agreement between the

53   AIRS OLR and CERES OLR data sets therefore serves to validate both OLR data sets

54   and indicates that neither data set contains spurious drifts. The agreement between

55   the AIRS OLR and CERES OLR data sets also validates, to some extent, values and

56   short-term trends of the AIRS retrieved geophysical parameters used in the

57   computation of AIRS OLR. The temporal and spatial variability of AIRS retrieved

58   geophysical parameters help explain those of OLR.

59   1.0 Introduction

60   This paper compares monthly mean values of the AIRS Version-6 Outgoing

61   Longwave Radiation (OLR) data set and the CERES_EBAF Edition 4.0 OLR data set

62   over a 14-year overlap period, September 2002 through August 2016. OLR, the

63   residual between incoming solar radiation and the sum of outgoing longwave (LW)

64   and reflected shortwave (SW) radiation, is an important component of the Earth's

65   energy imbalance. The Earth's climate will warm or cool depending on the sign and

66   magnitude of its energy imbalance.

67   Chu and Wang (1997), Soden and Held (2006), Soden et al. (2008), Dessler et al.

68   (2008), Huang and Ramaswamy (2009), Chung et al. (2010), Dessler (2010),

69   Zelinka and Hartmann (2011), Zelinka et al. (2012a), (2012b), and Vonder Haar et

70   al. (2012) utilized the spatial and temporal variability of OLR in their studies of

71   climate processes. Kidson et al. (2002), Jones et al. (2004), Barlow et al. (2005),

72   Kiladis et al. (2005), Hoyos and Webster (2007), Wong et al. (2006), Chiodi and

73   Harrison (2010), Tian et al. (2010), Loeb et al. (2012), and Hartmann and Ceppi

74 (2013) all used OLR variability as a proxy for tropical convective activity to further

75 their understanding of climate processes. The new AIRS OLR and CERES OLR data

76 sets described in this paper provide an improved depiction to scientists of the

77 variability of OLR over the fourteen-year period under study. Other AIRS products

78 help to explain this variability in terms of the variability surface and atmospheric

79 parameters during this time-period.

80 Susskind et al. (2012) compared values of the monthly mean AIRS Version-5 OLR

81 data set, including anomaly time series over the period September 2002 through

82 June 2011, with analogous results contained in the CERES Edition 2.6r OLR data set.

83 Susskind et al. (2012) showed that while there were biases between the AIRS OLR

84 and CERES OLR monthly mean data sets they used, the AIRS OLR and CERES OLR

85 anomaly time series, including short-term trends over the period September 2002

86 through June 2011, matched each other very closely on a 1°x1° spatial scale.

87 Following the methodology of Susskind et al. (2012), this paper compares ARCs

88 (Average Rates of Change) and ENCs (El Niño Correlations) of AIRS OLR anomaly

89 time series with those of CERES OLR. The ARC of an anomaly time series is the slope

90 of the linear least squares fit to the anomaly time series over the time-period under

91 study, and the ENC of an anomaly time series is its temporal correlation with an El

92 Niño Index (ENI). Susskind et al. (2012) defined the ENI as the difference of the

93 NOAA monthly mean oceanic Sea Surface Temperature (SST), averaged over the

94 NOAA Niño-4 spatial region extending from 5°N to 5°S longitude and from 160°E

95 eastward to 150°W, from an eight year climatology which Susskind et al. (2012)

96   generated. This paper redefines the ENI with regard to both the spatial and time

97   domains. We now define the ENI to include the average NOAA SST anomalies over

98   the combined Niño-4 and Niño-3 spatial regions, again extending from 5°N to 5°S

99   latitude and now extending from 160°E longitude further eastward to 90°W

100   longitude. We further extended the spatial domain of the ENI in this paper because

101   the center of El Niño/La Niña activity shifted eastward into the Niño-3 spatial

102   domain over the latter part of the fourteen-year time-period under study. We now

103   define monthly mean values of the ENI, as well as anomalies of all geophysical

104   parameters, as monthly mean differences from their fourteen-year climatologies.

105   This paper differs from in Susskind et al. (2012) in two very important ways

106   regarding the data sets used. AIRS flies on EOS Aqua and takes observations in

107   ascending orbits nominally at 1:30 PM local time and in descending orbits nominally

108   at 1:30 AM local time. Separate $AIRS_{PM}$ and $AIRS_{AM}$ data sets exist based on

109   observations made only in those orbits. Susskind et al. (2012) only examined

110   characteristics of an AIRS OLR data set derived using observations taken on both

111   sets of orbits. In this paper, we examine characteristics of $AIRS_{PM}$ and $AIRS_{AM}$ data

112   sets separately, as well as characteristics of a data set derived using observations

113   taken on both sets of orbits, $AIRS_{AVG,}$ as done by Susskind et al. (2012). In addition,

114   we now use the improved AIRS and CERES OLR data sets, AIRS/AMSU Version-6 and

115   CERES_EBAF (Energy Balanced and Filled) Edition 4.0.

116   The methodology used to produce CERES_EBAF Edition 4.0 OLR involves combining

117   CERES observations on the Terra and Aqua satellites with imager observations from

4

118   Geostationary (GEO) satellites in order to account for hourly Top_of_Atmosphere

119   (TOA) flux variations throughout the day in every region over an entire month

120   (Doelling et al., 2013; Loeb et. al., 2018). The AIRS Version-6 OLR product uses

121   observations taken only in the Aqua orbit. Consequently, even with perfect AIRS and

122   CERES OLR data products, one would still expect differences between the AIRS$_{AVG}$

123   OLR data set and the CERES OLR data set resulting from differences in temporal

124   sampling. This is especially true over land in locations in which Aqua does not

125   sample during times of maxima and minima of either land surface skin temperature

126   or of convection. The AIRS$_{PM}$ OLR and AIRS$_{AM}$ OLR data sets show areas, especially

127   over ocean, in which day/night OLR differences are very small. Direct comparisons

128   of the AIRS$_{AVG}$ OLR with CERES OLR data sets are therefore most meaningful in

129   those regions.

130   2.0 The AIRS Version-6 OLR and CERES_EBAF Edition 4.0 OLR Data Sets

131   2.1 AIRS Version 6-OLR

132   AIRS is a high spectral resolution infrared (IR) atmospheric sounder flying on the

133   Earth Observing System (EOS) Aqua satellite, alongside CERES and the microwave

134   (MW) sounders AMSU A1/A2. AIRS/AMSU Version 6 uses both AIRS and AMSU

135   radiances in the generation of products. The AIRS/AMSU Version-6 data set,

136   henceforth referred to as AIRS Version 6, began in September 2002 and extends

137   through August 2016, after which AMSU A2 ceased to function. AIRS Version-6

138   generates Level-2 values of AIRS OLR for each AIRS Field of View (FOV) as a

139   function of the AIRS retrieved geophysical state in that FOV via use of an OLR

140   Radiative Transfer Algorithm (RTA). AIRS/AMSU Version-6 uses no information

141   other than the AIRS/AMSU radiances in the generation of AIRS retrieved products

142   and OLR, with the exception of a 6 hour forecasted surface pressure, used in the

143   calculations of expected channel radiances as a function of geophysical parameters,

144   as well as in the calculation of AIRS OLR for a geophysical state.

145   The AIRS Version-6 OLR product has improved considerably compared to that of

146   AIRS Version-5 for two major reasons. The first is that the AIRS Version-6 retrieved

147   geophysical states (Susskind et al., 2014) are more accurate than the AIRS Version-5

148   geophysical states (Susskind et al., 2011). In addition, the AIRS Version-6 OLR RTA

149   (Iacono et al., 2008) is considerably more accurate than the OLR RTA (Mehta and

150   Susskind 1999a, Mehta and Susskind 1999b) used in Version-5.

151   We describe the methodology used to compute AIRS OLR in detail in Appendix A.

152   Appendix A shows that values of AIRS OLR in a FOV are linear combinations of

153   OLR_{CLR}, the value of OLR computed for the clear portion of the FOV, and OLR_{CLD}, the

154   OLR computed for different cloudy portions of the FOV. OLR_{CLR} increases with

155   increases in the earth's skin surface temperature T_s, with increases in the earth's

156   surface skin spectral emissivity ε_ν, and with increases in the atmospheric

157   temperature profile $T(p)$. On the other hand, OLR_{CLR} generally decreases with

158   increases in the atmospheric water vapor profile $q(p)$, especially in the mid-upper

159   troposphere. Values of OLR_{CLR} also depend on the vertical distributions of trace

160   gases such as O_3, CH_4, CO_2, and CO. OLR_{CLD} depends on these same geophysical

161   parameters, and also strongly depends on the heights, amounts, and spectral

6

162   emissivities of multiple layers of cloud cover as seen from above in the FOV,

163   especially those of high clouds. Appendix A explains why AIRS Version-6 determines

164   only the product of the fractional cloudiness α as seen from above in different FOVs,

165   and ε the cloud emissivity. We call this product $\alpha\varepsilon$ the "Radiative Effective Cloud

166   Fraction".

167   AIRS Version-6 generates single FOV Level-2 (L2) values of OLR under all cloud

168   conditions in which the cloud parameter retrieval in that FOV has converged. This

169   convergence occurs close to 100% of the time. All generated L2 values of AIRS OLR

170   are included in the AIRS gridded Level-3 (L3) OLR product.

171   The methodology used to compute AIRS OLR involves a sum of separate calculations

172   performed in each of 16 spectral bands. Table A1 in the Appendix shows that almost

173   half of OLR originates from bands with frequencies lower than 650 cm^{-1}, the lowest

174   frequency observed by AIRS. Table A1 also shows that LW flux at these lower

175   frequencies is relatively insensitive to cloud characteristics because, on the average,

176   the presence of clouds decreases OLR by a total of only 4.8 W/m^2 over those

177   frequencies not observed by AIRS. We obtained the AIRS Version-6 data set from

178   the Goddard Earth Sciences (GES) Data and Information Services Center (DISC)

179   doi:10.5067/Aqua/AIRS/DATA319.

180

181   2.2 CERES EBAF Edition 4.0 OLR

182   The CERES_EBAF Edition 4.0 data set began in March 2000 and, at the time of this

183   writing, extends through November 2019. CERES instruments fly on EOS Terra in a

184   sun-synchronous orbit with a descending mode equator crossing time of 10:30 AM

185   local time, as well as on EOS Aqua, alongside AIRS, in a sun-synchronous orbit with

186   an ascending mode equator crossing time of 1:30 PM local time. Each CERES

187   instrument measures filtered radiances in three distinct bands: the shortwave band

188   (SW), with wavelengths between 0.3 and 5 μm; the total band (TOT), with

189   wavelengths between 0.3 and 200 μm; and the window band (WN), with

190   wavelengths between 8 and 12 μm. Unfiltered SW, LW, and WN radiances are

191   determined following Loeb et al. (2001). CERES LW radiances are determined by

192   subtracting the CERES SW band radiances from the CERES TOT radiances. The

193   CERES-EBAF Edition 4.0 OLR product utilizes the CERES SYN 1deg Ed-4.0 LW data

194   product that combines observations from CERES instruments on each of the Terra

195   and Aqua satellites with geostationary imager measurements (Doelling et al., 2013)

196   in order to provide TOA fluxes hourly in 1°x1° latitude-longitude regions.

197   The CERES_EBAF Edition 4.0 data set utilizes an objective constrainment algorithm

198   described in Loeb et al. (2018). This approach makes a one-time adjustment to SW

199   and LW TOA fluxes, within their ranges of uncertainty, to remove inconsistencies

200   between the 10-year (July 2005-June 2015) average CERES all-sky global net TOA

201   flux and heat storage in the Earth-atmosphere system based on findings using in-

202   situ data. We obtained the CERES EBAF_Edition 4.0 OLR data set from

203   https://ceres.larc.nasa.gov/products-info.php?product=EBAF.

204   3.0 Inter-comparison of AIRS and CERES OLR Data Records

205   This section compares monthly mean values of fourteen years of the three AIRS

206   Version 6 OLR data sets and the CERES_EBAF Edition 4.0 OLR data set with each

207   other on a number of different spatial domains: global; the Northern Hemisphere

208   extra-tropics (NHET) 90°N-30°N; the tropics 30°N-30°S; and the Southern

209   Hemisphere extra-tropics (SHET) 30°S-90°S. The tropics represent 50% of the area

210   of the earth, and the NHET and SHET each represent 25% of the earth's area.

211   Figures 1a-1d show Version-6 monthly mean values, starting from the beginning of

212   the AIRS data set September 2002, of $AIRS_{PM}$ OLR, $AIRS_{AM}$ OLR, $AIRS_{AVG}$ OLR, and

213   CERES_EBAF Edition 4.0 OLR in four spatial domains. The vertical black lines mark

214   results for each January, and the numbers indicate the calendar year between each

215   January. Figure 1a shows results for global mean values of OLR. All global mean OLR

216   data sets contain a large seasonal cycle as well as a pronounced diurnal signal. AIRS

217   global mean OLR is greater at roughly 1:30 PM local time (pink) than it is at roughly

218   1:30 AM (red). This is because, everything else being equal, OLR increases with

219   increasing surface and atmospheric temperatures, both of which tend to be largest

220   in the afternoon. In the global mean sense, $AIRS_{AM}$ OLR matches CERES OLR almost

221   perfectly, while $AIRS_{PM}$ OLR is larger than CERES OLR. We later show this finding to

222   be the result of cancellation of positive and negative differences between $AIRS_{AM}$

223   OLR and CERES OLR in different spatial domains. $AIRS_{AVG}$ OLR values (blue) lie

224   between those of $AIRS_{AM}$ and those of $AIRS_{PM}$.

225   Figures 1b-d show analogous results for tropical mean OLR, NHET mean OLR, and

226   SHET mean OLR respectively. AIRS and CERES tropical mean OLR time series show

227   similar relative differences compared to those of global mean OLR. $AIRS_{AM}$ tropical

228   mean OLR again matches that of CERES almost perfectly, and $AIRS_{PM}$ tropical mean

229   OLR is larger than CERES tropical mean OLR. Tropical mean OLR has a seasonal

230   variability, with minima in January and maxima in July, but with a significantly

231   smaller and more complex seasonal cycle than that of global mean OLR. NHET and

232   SHET area mean OLR time series each show pronounced out of phase seasonal

233   cycles having maxima in local summer and minima in local winter. The NHET OLR

234   seasonal cycle is larger than that of the SHET. Consequently, the global mean OLR

235   seasonal cycle is in phase with, but smaller than, that of NHET.

236   The time of day dependences of the NHET and SHET AIRS OLR time series are more

237   complex than those of either global mean OLR or tropical mean OLR, as are the

238   relationships between AIRS OLR and CERES OLR.   The amplitudes of OLR diurnal

239   differences are considerably larger in the NHET, which is predominantly land, than

240   they are in the SHET, which is predominantly ocean. This phenomenon occurs

241   because oceanic surface skin temperatures have both smaller seasonal cycles and

242   smaller diurnal cycles than those for land.

243   Figures 2a-d present the differences (AIRS minus CERES) between the AIRS and

244   CERES monthly mean area mean OLR values shown in Figures 1a-d. Global mean

245   values of $AIRS_{AM}$ OLR match those of CERES OLR extremely closely in every month of

246   the time-period under study. Global mean values of $AIRS_{PM}$ OLR exceed those of

247 CERES OLR by about 7W/m^2. This bias has a small seasonal cycle, with minima in

248 Northern Hemisphere winter. The tropics contain similar, but somewhat larger,

249 differences between the time of day dependent AIRS OLR data sets and the CERES

250 OLR data set.

251 Levels of agreement between monthly mean values of AIRS OLR and CERES OLR

252 show different characteristics in the extra-tropics however. Figure 2c shows a

253 roughly out of phase NHET relationship of the seasonal cycle differences between

254 AIRS$_{PM}$ OLR and CERES OLR on the one hand (pink), and between AIRS$_{AM}$ OLR and

255 CERES OLR on the other hand (red). NHET AIRS$_{AM}$ area mean values of OLR match

256 those of CERES OLR almost perfectly during local winter, but are slightly negative

257 compared to CERES OLR during local spring/summer when the positive biases

258 between AIRS$_{PM}$ OLR and CERES OLR are largest. In the SHET, AIRS$_{AM}$ OLR matches

259 CERES OLR almost perfectly in local spring/summer, but is larger than CERES OLR

260 during local fall/winter. A consequence of the hemispheric asymmetries in the

261 AIRS$_{AM}$ and AIRS$_{PM}$ OLR differences from CERES OLR is that the AIRS$_{AVG}$ OLR time

262 series has only very small seasonal cycle differences from that of CERES OLR in each

263 extra-tropical region.

264 Table 1 shows the biases between monthly mean values of AIRS OLR and CERES

265 OLR for each spatial domain, as well as their temporal standard deviations (STDs).

266 Table 1 also includes the slopes of the linear least squares fits to the differences

267 between AIRS OLR and CERES OLR (W/m^2/yr), along with their uncertainties,

268 which represent twice the STDs of the linear least squares fits to the time series. The

269   biases between area-mean values of AIRS$_{AM}$ OLR and CERES OLR are smallest in all

270   spatial regions. Area mean biases do not tell the whole story, however. The

271   temporal STDs of the time series differences between AIRS OLR and CERES OLR are

272   in general smallest for AIRS$_{AVG}$ OLR, especially in the extra-tropics, with values

273   varying from 0.25 W/m^2 to 0.37 W/m^2 in all regions. This indicates that up to a bias,

274   the AIRS$_{AVG}$ OLR and CERES OLR time series agree best over all seasons and over

275   time. The differences between the AIRS$_{AVG}$ OLR time series and that of CERES OLR

276   have at most very small drifts in time in all spatial domains.

277   3.1 Inter-comparison of AIRS OLR and CERES OLR Monthly Climatologies

278   We generated climatologies for AIRS$_{AM}$ OLR, AIRS$_{PM}$ OLR, and CERES OLR for each

279   month of the year, on a 1°x1° spatial scale, by taking the monthly mean averages of

280   OLR in that grid box over the fourteen-year period under study. We generated

281   AIRS$_{AVG}$ OLR climatologies by first taking the average of the monthly mean AIRS$_{PM}$

282   and AIRS$_{AM}$ OLR products for each month and subsequently producing analogous

283   AIRS$_{AVG}$ climatologies for that month.

284   Figures 3a and 3b show the spatial distributions of the January AIRS$_{AVG}$ OLR

285   climatology and of the January CERES OLR climatology respectively. The statistics

286   on each figure indicate the area weighted global mean value of each field as well as

287   its area weighted spatial STD. January climatological OLR values are very low at high

288   latitudes where surface skin temperatures and atmospheric temperatures are both

289   low. Very low OLR climatological values also occur in some tropical areas that

290   contain large amounts of high clouds resulting from significant convective activity in

291   these regions. Such areas also tend to contain large amounts of Mid-Upper

292   Tropospheric Humidity (MUTH), which, like high cloud cover, also lowers OLR,

293   though to a lesser extent.   Figures 3c-e show respectively the spatial differences

294   from the January CERES OLR climatology of the January $AIRS_{AVG}$, $AIRS_{AM}$, and $AIRS_{PM}$

295   OLR climatologies from the January CERES OLR climatology, and Figure 3f shows

296   the differences between the January $AIRS_{PM}$ OLR climatology and the January

297   $AIRS_{AM}$ OLR climatology.

298   While January climatological values of $AIRS_{AM}$ OLR best match those of CERES OLR

299   in the global mean sense, the global mean match between values of $AIRS_{AM}$ OLR and

300   CERES OLR is very misleading. The January $AIRS_{AM}$ OLR climatology is somewhat

301   higher than that of CERES OLR over ocean, but is significantly lower than that of

302   CERES OLR over arid land, which cools considerably at night, with an area weighted

303   spatial STD of 4.19 W/m^2. Figure 3c shows that the spatial differences between the

304   January $AIRS_{AVG}$ OLR climatology and the January CERES OLR climatology are much

305   more homogeneous, with a spatial STD of 2.58 W/m^2. This result also demonstrates

306   that the AIRS OLR calculations treat the large effects of tropical clouds on OLR very

307   accurately.

308   The biggest differences between the January $AIRS_{AVG}$ OLR climatology and the

309   January CERES OLR climatology occur in areas in which the differences between the

310   January $AIRS_{PM}$ and $AIRS_{AM}$ OLR climatologies are largest, as shown in Figure3f.

311   AIRS and CERES temporal sampling differences are therefore a factor affecting the

312   spatial differences between the January $AIRS_{AVG}$ OLR and CERES OLR climatologies.

313   AIRS diurnal January OLR climatological differences are greater than 45 W/m^2 over

314   arid regions such as the Sahara Desert, the southern parts of South America and

315   South Africa, and Western Australia. The AIRS January OLR climatology in some

316   Southern Hemisphere tropical oceanic areas is actually somewhat lower at 1:30 PM

317   than it is at 1:30 AM. This is a result of increases in low cloud cover in these areas as

318   sampled by Aqua at 1:30 AM as compared to 1:30 PM.

319   Doelling et al. (2013) addressed ways to account for diurnal variability of OLR in a

320   CERES OLR product. His CERES GEO-combined method, used in CERES_EBAF

321   Edition 4.0, incorporates hourly imager data from five geostationary satellites to

322   help account for changes in OLR between CERES observation times. Harries et al.

323   (2005) obtained very good results using the CERES GEO-combined method, after

324   removing calibration differences for each CERES instrument, when compared to 15-

325   min resolution OLR as observed from Geostationary Earth Radiation Budget (GERB).

326   Using data for January 2005, Doelling et al. (2013) showed that the amplitude of the

327   OLR diurnal cycle can reach 35 W/m^2 over a Saharan desert location (30.5°N, 0.5°E),

328   over 8 W/m^2 in a marine stratus location (20.5°S, 10.5°E), and over 45 W/m^2 in a

329   land convective region (20.5°S, 20.5°E).

330   Figures 4a-f show analogous July OLR climatologies and climatological differences.

331   AIRS OLR diurnal differences in arid areas are in general larger in July than they are

332   in January in both hemispheres. As in January, the differences of $AIRS_{AVG}$ OLR from

333   CERES OLR are for the most part spatially homogeneous with the exception of land

334   areas containing very large diurnal differences of OLR.

335   4.0 Factors Contributing to Diurnal OLR Climatological Differences

336   Figures 3f and 4f depict diurnal differences of the AIRS January OLR climatology and

337   of the July OLR climatology, respectively. Positive OLR diurnal differences are

338   greatest over arid land in both seasons, with values that are largest in the tropics

339   and during local summer in the extra-tropics. Moderately positive diurnal OLR

340   differences also occur over elevated terrain in polar summer in Eastern Antarctica

341   (January) and over Greenland (July). Polar OLR diurnal differences are close to zero

342   in both months in local winter. Figure 5 shows diurnal climatological differences of

343   three AIRS derived geophysical parameters for January and July on which OLR

344   strongly depends: surface skin temperature T_s; Radiative Effective Cloud Fraction

345    $\alpha\varepsilon$; and 500 mb specific humidity $q(500)$. OLR increases with increases in T_s and

346   decreases with increases in $\alpha\varepsilon$ and with increases in $q(500)$. For this reason,

347   positive (negative) values of diurnal differences of T_s are shown in Figure 5 in

348   shades of red and green (blue and yellow), and the reverse color code is used for

349   diurnal differences of $\alpha\varepsilon$ and $q(500)$. Diurnal differences of T_s are always positive

350   and are largest over tropical and mid-latitude land, especially in local summer.

351   Moderately positive T_s diurnal differences also occur in polar summer over elevated

352   terrain such as Eastern Antarctica and Greenland. Analogous features appear in the

353   diurnal OLR differences shown in Figures 3f and 4f over land. This demonstrates

354   that diurnal T_s differences affect those of OLR in these regions. Diurnal T_s differences

355   are very small over ocean. Diurnal OLR differences over ocean result primarily from

356   diurnal $\alpha\varepsilon$ sampling differences

357   Over land, regions containing large positive diurnal T_s differences (red) often

358   contain large negative diurnal $\alpha\varepsilon$ differences (red). Reduction of cloud cover during

359   the day in these regions further enhances the positive temporal effect on OLR of

360   afternoon warming of land temperatures. One might think that afternoon values of

361    $\alpha\varepsilon$ over hot convective regions would be high because of increased afternoon

362   thunderstorm activity, but this phenomenon usually occurs closer to 3:30 PM local

363   time, a time AIRS does not observe. Diurnal OLR differences over some convective

364   regions are reduced to some extent by diurnal changes of opposite sign of *q(500)*.

365   5.0 Inter-comparison of AIRS OLR and CERES OLR Anomaly Time Series

366   Figure 6 shows anomaly time series of AIRS OLR and CERES OLR as a function of

367   time over the period September 2002 through August 2016. Figure 6a shows global

368   mean anomalies, Figure 6b shows tropical mean OLR anomalies, and Figures 6c and

369   6d show NHET and SHET OLR anomalies respectively. Diurnal differences between

370   AIRS OLR anomalies exist, but they are small compared to the anomalies themselves.

371   Figure 6b includes values of the ENI. Tropical mean OLR anomalies tend to track the

372   ENI to some extent. The positive tropical mean OLR anomalies in early 2003, in

373   2007, in early 2010, in 2015, and in early 2016, generally correspond to periods

374   with positive values of the ENI, during which there are positive T_s anomalies in the

375   combined Niño-3 and Niño-4 regions. This is especially true in 2015 and 2016. The

376   negative tropical OLR anomalies in 2006, in 2007, in 2008, and in mid-2010 to early

377   2012, generally correspond to periods with negative values of the ENI, during which

378   there are negative T_s anomalies in the combined Niño-3 and Niño-4 regions. Figure

379   6b indicates that tropical mean OLR anomalies tend to lag the ENI by a small amount

380   in time. The unlagged temporal correlation of tropical mean OLR anomalies with the

381   ENI is 0.55. The temporal correlation of tropical mean OLR anomalies with the ENI

382   is largest after a lag of OLR by two months from the ENI, with a lagged temporal

383   correlation of 0.64. Global mean OLR anomalies also track the ENI to some extent

384   because the tropics constitute 50% of the globe.

385   NHET OLR anomalies contain a substantial positive peak in early 2016, as do

386   tropical mean and global mean OLR anomalies. Such positive anomalies in early

387   2016 do not occur in the SHET OLR anomaly time series.

388   5.1 Comparison of ARCs of AIRS OLR and CERES OLR

389   Table 2 presents area mean ARC's (W/m^2/yr) of all AIRS OLR anomaly time series,

390   as well as those of CERES OLR. ARCs of all AIRS OLR anomaly time series show

391   excellent agreement with those of CERES in all regions. This indicates that there was

392   essentially no drift between the AIRS and CERES OLR data sets over the 14-year

393   time period studied.

394   Global mean OLR ARCs are all very slightly positive, with values that are within their

395   uncertainties. Tropical mean OLR ARCs are all slightly negative, again with values

396   within their uncertainties. SHET OLR ARCs are all essentially zero. On the other

397   hand, NHET OLR ARCs are all very positive over this time-period and have values

398   considerably larger than their uncertainties. This finding is the result of the large

399   NHET positive OLR anomalies that occurred in early 2016. The existence of the

400   small positive global mean value of OLR ARCs arises primarily from those in the

401   NHET, which represents 25% of the area of the globe.

402   With the exception of the SHET, which contains little land, $AIRS_{PM}$ OLR ARCs are all

403   more negative, or less positive, than $AIRS_{AM}$ OLR ARCs. While the area mean

404   differences between $AIRS_{PM}$ and $AIRS_{AM}$ OLR ARCs are within their uncertainties,

405   these differences are not a result of random noise and are a physical result

406   discussed later.

407   ARCs of any geophysical parameter can be time-period dependent. Su et al. (2017)

408   analyzed AIRS data through December 2013 and showed a significant negative

409   tropical mean OLR trend of approximately -1.0 W/m^2/decade. The negative short-

410   term OLR trend Su et al. (2017) observed was a result of the 2013 La Niña event that

411   took place near the end of the time-period they studied.

412   5.2 Spatial Distributions of ARCs and ENCs of AIRS and CERES OLR

413   Figures 7a and 7b show the spatial distributions on a 1° latitude by 1° longitude grid

414   of the ARCs of $AIRS_{AVG}$ OLR and CERES OLR. All grid point values shown in these and

415   subsequent spatial plots have a three-point smoother applied to them in both the

416   latitude and longitude domains. Reds and greens show positive OLR ARCs and blues

417   and yellows show negative OLR ARCs. At least as significant as the values of the OLR

418   ARCs shown in Figures 7a and 7b are their very coherent spatial structures, which

419   are virtually indistinguishable from each other. These figures, and all subsequent

420   spatial plots, contain a black box surrounding the NOAA Niño-4 region and a gray

421   box surrounding the NOAA Niño-3 region.

422   While all global mean and tropical mean OLR ARCs are essentially zero within their

423   uncertainties, there is considerable spatially coherent structure in the ARCs of OLR,

424   especially in the tropics. In particular, there are large negative OLR ARCs

425   surrounding the equator in the region 160°W eastward to 70°W, indicating that OLR

426   has decreased in this region over the time-period under study. Smaller, but

427   significant, positive OLR ARCs exist in equatorial areas westward and eastward of

428   this region that compensate for those negative values in the tropical mean sense.

429   Figure 7c shows the spatial differences between the ARCs of $AIRS_{AVG}$ OLR and those

430   of CERES OLR. The area weighted spatial correlation between the two sets of OLR

431   ARCs is 0.978, and the spatial STD of their differences is 0.047 $W/m^2/yr$. $AIRS_{AVG}$

432   OLR ARCs tend to be slightly more positive (or less negative) than those of CERES

433   over tropical oceans, and more negative (or less positive) than those of CERES over

434   the Sahara Desert, Saudi Arabia, and Australia. The area weighted global mean ARC

435   of $AIRS_{AVG}$ OLR for this period is 0.005 $W/m^2/yr$ less positive than that of CERES.

436   Figure 7d shows the spatial differences between the ARCs of $AIRS_{PM}$ OLR and those

437   of $AIRS_{AM}$ OLR. The largest diurnal differences of ARCs of AIRS OLR occur over

438   Australia. Therefore, temporal sampling differences may be a factor affecting the

439   small differences between the ARCs of $AIRS_{AVG}$ OLR and those of CERES OLR over

440   Australia. Unlike over land, diurnal differences of $AIRS_{AVG}$ OLR ARCs are scattered

441   over ocean. This is primarily the result of sampling differences of cloud cover as

442   observed separately during the ascending and the descending orbits of Aqua.

19

443   Figures 7e and 7f show patterns of the ENCs of the AIRS$_{AVG}$ OLR and of the CERES

444   OLR anomaly time series. ENCs represent correlations and are therefore unit-less,

445   with values ranging from -1.0 to 1.0. Reds and greens indicate spatial regions with

446   positive ENCs, in which anomalies at a given time tend to be of the same sign as the

447   ENI, while blues and yellows indicate regions with negative ENCs in which the

448   reverse is true. As with ARCs, there is excellent agreement between the spatial

449   patterns of the ENCs of AIRS$_{AVG}$ OLR and the ENCs of CERES OLR. OLR ENCs can be

450   very large in the tropics, especially within the Niño-4 region in which they are very

451   negative. This indicates that OLR typically has negative anomalies within the Niño-4

452   region during El Niño conditions and positive anomalies within the Niño-4 region

453   during La Niña conditions.

454   While there are similarities between the patterns of ARCs and ENCs of OLR in the

455   tropics, there are also some significant differences between them. Unlike OLR ARCs,

456   which have both positive and negative values within the Niño-4 region, ENCs of OLR

457   have large negative values within the entire Niño-4 region. In addition, ENCs of OLR

458   are small and have mixed signs within the Niño-3 region while ARCs of OLR are

459   large and negative within in this region.

460   The differences in signs and relative magnitudes in the tropics with regard to ARCs

461   of OLR on the one hand, and ENCs of OLR on the other hand, are a result of when

462   and where El Niño/La Niña activity took place during the period under study. As will

463   be shown later, most El Niño/La Niña activity took place within the Niño-4 region,

464   and it occurred primarily in the early to middle part of the time-period under study.

465 Consequently, the large negative OLR ENCs found within the Niño-4 region do not

466 occur within the Niño-3 region.

467 In the absence of other changes, OLR increases with increasing T_s, which, by

468 definition, has a positive correlation with the ENI within the Niño-4 region.

469 Therefore, one might expect to have positive OLR ENCs within the Niño-4 region.

470 The effect of local increases (decreases) of T_s on OLR within the Niño-4 region at a

471 given time is more than offset by corresponding local increases (decreases) in both

472 high cloud cover and MUTH, each of which decreases (increases) OLR. Areas

473 surrounding Niño-4 to the north and south have positive OLR ENCs. This indicates

474 that convective activity in those areas tended to increase (decrease) during periods

475 when it decreased (increased) within the Niño-4 region.

476 6.0 ARCs and ENCs of Important Geophysical Parameters Affecting OLR

477 Computed values of AIRS OLR in a FOV depend on the AIRS retrieved geophysical

478 state in that FOV. Therefore, one can attribute ARCs and ENCs of AIRS OLR to those

479 of the AIRS retrieved surface and atmospheric geophysical parameters. It is

480 impractical to discuss relevant results of all the geophysical parameters affecting

481 OLR. In this paper, for demonstrative purposes, we concentrate on surface skin

482 temperature T_s; surface air temperature T_{sa}; 500 mb specific humidity $q(500)$; and

483 Radiative Effective Cloud Fraction $\alpha\varepsilon$. Figure 8a shows the spatial distribution of

484 ARCs of AIRS$_{AVG}$ T_s. The color code in Figure 8a is analogous to that used in Figure

485 7a, with positive values depicted in reds and greens and negative values depicted in

486 blues and yellows. In the global mean sense, T_s warmed at a rate of 0.019K/yr over

487   the 14-year time period under study. While this increase is consistent with "global

488   warming", the earth has not warmed uniformly over the time-period under study.

489   The earth's surface has warmed considerably poleward of 70°N, especially west of

490   the dateline, as well as in an area centered at 50°N and 40°E. There has also been

491   slight warming during this period over some tropical oceanic areas, especially

492   within the Niño-3 region. On the other hand, there has been considerable cooling

493   during this period over Greenland and the ocean surrounding it, as well as over

494   Eastern Australia and over some oceanic areas poleward of 60°S.

495   OLR increases with increasing T_s, everything else being equal. Consequently,

496   features of ARCs of T_s will look like those of ARCs of OLR to the extent that changes

497   in T_s are the driving force behind changes in OLR. Features of T_s ARCs in mid-high

498   latitudes are readily apparent in those of OLR ARCs. Therefore, changes in OLR over

499   time in these regions resulted primarily from changes in T_s. Note, in particular, the

500   in-phase relationship poleward of 60°N between the ARCs of OLR and the ARCs of T_s.

501   Figure 8b shows ARCs of T_{sa} using the same color scale as in Figure 8a. While OLR

502   depends significantly on T_s, it depends very little on T_{sa}. Nevertheless, we show T_{sa}

503   because surface air temperature represents the environment in which we live. ARCs

504   of T_{sa} are very similar to those of T_s, but are somewhat smaller and are smoother in

505   space. Globally, surface air temperature warmed at a rate of 0.16K/yr, which is

506   slightly less than that of surface skin temperature.

507   Figures 8c and 8d show ARCs of $q(500)$ and ARCs of $\alpha\varepsilon$ respectively. Global mean

508   ARCs of $q(500)$ and $\alpha\varepsilon$ are each positive. This indicates that AIRS shows that the

509   Earth has both moistened in the middle troposphere during the time-period under

510   study and has gotten somewhat cloudier over this time-period as well. A

511   comparison of Figures 7a and 8c demonstrates that the spatial distribution of

512   tropical ARCs of *q(500)* is virtually identical to that of OLR, albeit with an opposite

513   sign. This shows that temporal changes in tropical OLR are closely related to those

514   of *q(500)*. The spatial agreement between ARCs of OLR with ARCs of $\alpha\varepsilon$ is not as

515   good as it is with ARCs of *q(500)* because cloud fraction, as shown, refers to total

516   cloud cover, independent of cloud top pressure. ARCs of $\alpha\varepsilon$ for high clouds (not

517   shown) gives a closer spatial agreement with ARCs of OLR.

518   Figures 9a-d show the spatial distributions of ENCs of $AIRS_{AVG}$ T_s, T_{sa}, *q(500)*, and $\alpha\varepsilon$

519   respectively. Figure 9a shows that the largest correlations of T_s with the ENI occur in

520   the tropics. As expected, T_s anomalies have large positive correlations with the ENI

521   over each of the Niño-4 and Niño-3 regions. Figure 9a shows that T_s anomalies also

522   have positive correlations with the ENI, though less so, in areas immediately to the

523   north and south of the Niño-4 and Niño-3 regions, and that these areas containing

524   positive T_s correlations with the ENI extend to the west coasts of the United States

525   and Canada. Regions to their north, south, and west contain significant negative

526   correlations of T_s with the ENI. The spatial distributions of ENCs of T_s and ENCs of

527   T_{sa} are very similar to each other, but the magnitudes of ENCs of T_s are somewhat

528   larger than the magnitudes of ENCs of T_{sa}.

529   In the tropics, spatial patterns of ENCs of *q(500)* are similar to those of ENCs of T_s

530   and ENCs of T_{sa} because periods of locally warmer (cooler) surface temperatures

531   tend to correspond to periods of locally moister (drier) mid-tropospheres. Tropical

532   OLR ENCs, shown in Figure 7c, are for the most part anti-correlated with ENCs of

533    $q(500)$ because local increases in $q(500)$ result in local decreases in OLR. Tropical

534   ENCs of $\alpha\varepsilon$ show some similarity to those of $q(500)$ but with significant differences,

535   particularly within the Niño-3 region and also off the west coast of North America.

536   7.0 Hovmöller Diagrams

537   Hovmöller diagrams are plots of anomalies of geophysical parameters integrated

538   over a range of latitudes as a function of time and longitude. Figure 7e shows that

539   the largest correlations and anti-correlations of OLR with the ENI occur near the

540   equator, in a region extending from 100°E longitude eastward to 80°W longitude.

541   Hovmöller diagrams help explain the factors affecting this feature. Figures 10a-10d

542   show monthly mean Hovmöller Diagrams of T_s, OLR, 500 mb specific humidity, and

543    $\alpha\varepsilon$ integrated over the latitude range 5°N through 5°S (vertical scale) in each 1°

544   longitude bin (horizontal scale) for the time-period September 2002 through

545   August 2016. We applied a 5 point (5 month) linear smoothing in the vertical and a

546   15-point (15 degree) linear smoothing in the horizontal in order to minimize the

547   effects of small discontinuities between adjacent rectangular grid points on the

548   figures. Most of the Hovmöller domain is ocean. There are three relatively small land

549   areas near the equator: South America, Africa, and Indonesia. These land areas each

550   lie between the three sets of black vertical lines indicated in Figures 10a-10d. The

551   three adjacent vertical gray lines in Figure 10 indicate the longitudinal extents of the

552   Niño-4 region and Niño-3 region respectively.

553   Figure 10a depicts positive T_s anomalies in shades of red and yellow, and negative T_s

554   anomalies in shades of blue and purple. The largest equatorial T_s anomalies

555   occurred over the ocean between 160°E, the western edge of the Niño-4 region, and

556   90°W, the eastern edge of the Niño-3 region, and sometimes extended further

557   eastward to 80°W off the west coast of South America. Significant El Niño events

558   (dark red and yellow) occurred within the Niño-4 region in 2003, 2010, 2015, and

559   2016, and significant La Niña events (dark blue and purple) occurred within the

560   Niño-4 region in 2008 and 2011. The El Niño event beginning in mid-2015 differs in

561   location from the earlier El Niño events in that it occurred primarily within the

562   Niño-3 region and extended to the west coast of South America.

563   Figure 10b depicts the Hovmöller diagram of OLR. Figure 10b demonstrates that

564   equatorial OLR anomalies are highly anti-correlated with T_s anomalies within the

565   Niño-4 region. The same result occurs within the Niño-3 region to some extent after

566   mid-2015. Figures 10a and 10b explain why OLR anomalies within the Niño-4

567   region are highly anti-correlated with the ENI. ENCs of OLR within the Niño-3 region

568   are smaller than they are within the Niño-4 region, and can be positive or negative,

569   because OLR anomalies within the Niño-3 region have a lower correlation with the

570   ENI in the early part of the time-period, during which T_s anomalies occurred

571   primarily within the Niño-4 region.

572   Figures 10c and 10d show analogous Hovmöller diagrams of $q(500)$ and $\alpha\varepsilon$

573   respectively. Anomaly patterns of $q(500)$ within the Niño-3 and Niño-4 regions

574   generally follow those of T_s very closely, both in relative magnitudes and phase. This

575 demonstrates that positive (negative) SST anomalies correspond to periods of

576 locally increased (decreased) convection, which in turn lead to enhancement

577 (suppression) of $q(500)$. These periods often correspond to periods of increased

578 (decreased) high cloud cover (not shown). Local values of OLR therefore decrease

579 (increase) during El Niño (La Niña) periods. Cloud cover as shown includes amounts

580 of low clouds. Such clouds are not associated convective activity.

581 8.0 Diurnal Differences of ARCs and ENCs of Relevant Geophysical Parameters

582 This section compares diurnal differences of the ARCs and ENCs of AIRS OLR with

583 those of select geophysical parameters on which OLR depends. Figures 11a-c show

584 the spatial distributions of the ARCs of $AIRS_{PM}$ T_s, of the ARCs of $AIRS_{AM}$ T_s, and of the

585 difference between their ARCs ($AIRS_{PM}$ minus $AIRS_{AM}$) respectively. The spatial

586 features of the PM/AM differences of OLR ARCs, shown in Figure 7d, tend to match

587 those of Figure 11c in both signs and relative magnitudes in places over land where

588 both sets of diurnal differences are large. This shows that over land, diurnal

589 differences of ARCs of T_s are a significant factor affecting the diurnal differences of

590 ARCs of OLR. Figure 11d shows the diurnal differences of ARCs of $q(500)$, which

591 contain only small-scale features that occur primarily over ocean. These features are

592 most likely a result of sampling differences of anomalies over the month as observed

593 by AIRS at 1:30 PM and at 1:30 AM respectively.

594 Figures 12a-d are analogous to Figures 11a-d, but with regard to ENCs of the same

595 geophysical parameters. ENCs of T_s at 1:30 PM are very positive over Australia in

596 those regions in which 1:30 PM ARCs of T_s are very negative. On the other hand,

597   ARCs and ENCs of T_s over Australia at 1:30 AM are each small. It is apparent that the

598   large negative diurnal differences of the ARCs of both T_s and of OLR in Australia are

599   the result of positive correlations of T_s with El Niño/La Niña activity that occurred

600   during the day but did not occur appreciably at night. These differences are largest

601   over Eastern Australia, which we define as eastward of 140°E longitude. As with

602   ARCs, diurnal differences of ENCs *q(500)* have only very small spatial scales, related

603   primarily to sampling differences of *q(500)* observed at different times of day.

604   8.1 Diurnal differences of T_s Anomaly Time Series over Eastern Australia

605   Figures 13a-13c show monthly mean T_s anomaly time series over Eastern Australia

606   for 1:30 PM, for 1:30 AM, and for 1:30 PM minus 1:30 AM respectively. These figures

607   also contain the ENI multiplied by two. The Eastern Australia PM T_s anomaly time

608   series shows considerable high frequency monthly mean variability not found in the

609   ENI.   Nevertheless, there is a coarse in-phase relationship over Eastern Australia

610   between 1:30 PM T_s anomalies and the ENI, with a temporal correlation of 0.45.

611   There are positive PM T_s anomalies in 2002, 2005, late 2006, late 2009, early 2015,

612   and early 2016, which are all in phase with positive values of the ENI. Even more

613   significant are the negative PM T_s anomalies that occurred in late 2007, early 2008,

614   mid-late 2010, and 2011, which are in phase with negative values of the ENI. The

615   negative trend of Eastern Australian PM T_s anomalies observed over the time-period

616   under study is primarily the result of the large negative PM T_s anomalies that

617   occurred during the La Niña period from mid-2010 through late 2011. This implies

618   that daytime surface skin temperatures over Eastern Australia were significantly

619   cooler than normal during this large La Niña event.

620   The AM T_s anomaly time series over Eastern Australia is shown in Figure 13b. AM T_s

621   anomalies are much smaller than PM T_s anomalies, and have a correlation with the

622   ENI of only 0.11. This implies that unlike during the day, El Niño/La Niña events

623   had little effect on nighttime T_s anomalies over Eastern Australia. Figure 13c,

624   showing the difference between the Eastern Australian 1:30 PM and 1:30 AM T_s

625   anomalies, is similar in appearance to Figure 13a because AM T_s anomalies were

626   small as compared to PM T_s anomalies.

627   9.0 Summary

628   This paper compares the temporal and spatial characteristics of three monthly

629   mean L3 AIRS Version-6 OLR data sets AIRS$_{PM}$, AIRS$_{AM}$, and AIRS$_{AVG}$, with those of

630   the L3 CERES_EBAF Edition 4.0 OLR data set over a14-year overlap time-period of

631   the two data sets, September 2002 through August 2016. AIRS and CERES global

632   mean OLR time series both show pronounced annual cycles, with maxima in July

633   and minima in January. AIRS$_{AVG}$ OLR displays a positive bias as compared to CERES

634   OLR of roughly 3.0 W/m^2 with essentially no drift over the 14 years we compared.

635   At least part of the differences between the computed AIRS OLR product and the

636   observed CERES OLR product is a result of limitations in the AIRS OLR RTA, as well

637   as possible biases in the AIRS retrieved geophysical parameters used in the

638   computation of AIRS OLR. In addition, the CERES OLR product also has calibration

639   uncertainties. Temporal sampling differences in the data used by AIRS and CERES

640   contributed to this bias as well.

641   There is excellent agreement between the ARCs and ENCs of the $AIRS_{AVG}$ OLR

642   anomaly time series and the CERES OLR anomaly time series down to the 1° x 1°

643   spatial scale. The excellent agreement in space and time of the two independently

644   derived OLR data sets serves to validate each OLR data set in terms of both absolute

645   values and stability. This agreement also tends to validate the geophysical

646   parameters derived from the AIRS observations used in the computation of AIRS

647   OLR, and consequently, it allows for the explanation of OLR variability in terms of

648   the variability of geophysical parameters.

649   Fourteen year AIRS and CERES global mean OLR ARCs are essentially zero within

650   their stated uncertainties, defined as twice the STDs of the linear least squares fits to

651   their anomaly time-series. Both AIRS and CERES show, on the other hand, that

652   Northern Hemisphere extra-tropical OLR ARCs have positive values which agree

653   well with each other and are both larger than their uncertainties. This finding is the

654   result of the considerable warming that took place during the period under study

655   from the Greenwich Meridian westward toward the dateline poleward of 70°N.

656   The differences between the AIRS and CERES OLR climatologies, as well as between

657   the AIRS and CERES OLR anomaly time series, are each largest in a region in Eastern

658   Australia in which the ARCs and ENCs of $AIRS_{PM}$ T_s differ considerably from those of

659    $AIRS_{AM}$ T_s.

660

29

661

662   Appendix A

663   Observed AIRS channel radiances in a FOV depend on the surface, atmospheric and

664   cloud conditions within the FOV. To first order, AIRS observations do not

665   distinguish between upwelling radiation passing through the clouds, which depends

666   on the spectral emissivity of the clouds ε, and radiation coming from around the

667   sides of clouds, which depends on fractional cloud cover, α. Consequently, the

668   Version-6 AIRS cloud parameter retrieval algorithm only determines $\alpha\varepsilon$ the product

669   of these geophysical parameters. We refer to $\alpha\varepsilon$ as the Radiative Effective Cloud

670   Fraction.

671   A-1 Methodology used to compute OLR

672   The methodology used to compute AIRS Version-6 OLR is analogous to that used in

673   AIRS Version-5, but with some important differences. As with AIRS Version-5, AIRS

674   Version-6 assumes that an AIRS FOV contains up to two distinct layers of clouds as

675   seen from above, with cloud top pressures p_{c1} and p_{c2}. Consequently, OLR computed

676   in an AIRS FOV is given by the linear combination of the OLR arising from up to

677   three assumed possible scenes found in the FOV: OLR arising from the clear portion

678   of the scene; and OLR arising from each of the up to two cloudy portions of the scene,

679   covered by p_{c1} and p_{c2}

680          $$OLR = (1-\alpha\varepsilon_1-\alpha\varepsilon_2)\ OLR_{CLR} + \alpha\varepsilon_1 OLR_{CLD1} + \alpha\varepsilon_2 OLR_{CLD2} \qquad (A1)$$

681 As in Version-5 (Mehta and Susskind 1999a, 1999b), OLR in Version-6 is computed

682 as the sum of fluxes in each of m contiguous spectral bands. AIRS Version-6 uses the

683 Iacono et al. (2008) OLR RTA, which computes OLR_{CLR} as the sum of 16 spectral

684 components according to

685 $$OLR_{CLR} = \pi \sum_{m=1}^{16} \left[\varepsilon_m B(v_m, T_s) \tau_m(p_s) + \int_{\ln p_s}^{\ln \bar{p}} B(v_m, T(p)) \frac{d\tau_m(p)}{d\ln p} d\ln p \right] \quad (A2)$$

686 in which $B(v, T)$ is the Planck blackbody function evaluated at frequency v and

687 temperature T; v_m is the central frequency of spectral band m; ε_m is the mean

688 surface emissivity in band m; and $\tau_m(p)$ represents the effective band averaged

689 atmospheric transmittance in band m from pressure p to the top of the atmosphere

690 $\bar{p}$. The terms OLR_{CLD1} and OLR_{CLD2} used in Equation A1 are computed analogously to

691 OLR_{CLR}, but with p_s in Equation A2 being replaced by p_{c1} or $p_{c2.}$ The combined use of

692 Equations A1 and A2 makes the implicit assumption that cloud spectral emissivity is

693 independent of frequency.

694 The OLR RTA used in AIRS Version 6 (Iacono et al., 2008) has two very important

695 upgrades compared to Mehta and Susskind (1999a; 1999b) which is the OLR RTA

696 used in AIRS Version-5. The parameterization used in Iacono et al. (2008) was

697 generated using more up to date line absorption parameters, especially in the very

698 strong water vapor absorption band near 350 cm^{-1}. In addition, the Iacono et al.

699 (2008) OLR RTA accounts for the variability of additional atmospheric constituents

700 such as CO_2, CO, and CH_4 in the OLR calculation, while Mehta and Susskind (1999a,

701 1999b) assigned fixed mixing ratios of all trace gases except for water vapor and

702 ozone.

703   Table A1 shows the frequency domains of each of the 16 spectral bands used in

704   Equation A2. Table A1 includes the global mean annual mean individual spectral

705   band fluxes (W/m^2) of each spectral band and the percentage contribution of each

706   spectral band to total OLR. Table A1 also includes the spectral contribution of each

707   band to two other important geophysical parameters not previously discussed in

708   this paper, Clear Sky OLR (OLR$_{CLR}$) and Longwave Cloud Radiative Forcing (LCWRF).

709   LWCRF, the difference between OLR$_{CLR}$ and OLR, represents the effect of clouds on

710   OLR.

711   Almost half of OLR comes from spectral bands 1-3, extending from 100 cm^{-1} to 630

712   cm^{-1}. This is an extensive spectral domain in which AIRS does not make any

713   observations. The largest approximation made in the current methodology used in

714   the computation of AIRS OLR is that cloud spectral emissivity ε is frequency

715   independent. This assumption most likely does not hold at the longer wavelengths

716   of spectral bands 1-3, especially in the presence of cirrus clouds. The sixth column in

717   Table A1 shows that the presence of clouds in a FOV decreases total flux on the

718   average by about 4.8 W/m^2 in the longwave spectral domain not observed by AIRS.

719   The excellent results shown in this paper demonstrates that the approximation of

720   spectrally independent values of $\alpha\varepsilon$ made in the computation of AIRS OLR works

721   extremely well, at least on the average.

722

723

724

725

726 References

727 Barlow, M., M. Wheeler, B. Lyon, and H. Cullen (2005), Modulation of daily

728 precipitation over Southwest Asia by the Madden-Julian Oscillation, Mon. Weather

729 Rev., 133, 3579-3594.

730 Chiodi, A. M., and D. E. Harrison (2010), Characterizing warm-ENSO variability in the

731 equatorial Pacific: An OLR perspective, J. Clim., 23, 2428-2439.

732 Chu, P. S. and J. B. Wang (1997), Recent climate change in the tropical Western

733 Pacific and Indian Ocean regions as detected by outgoing longwave radiation

734 records, J. Clim., 10, 636-646.

735 Chung, E. S., D. Yeomans, and B. J. Soden (2010), An assessment of climate feedback

736 processes using satellite observations of clear-sky OLR, Geophys. Res. Lett., 37, 7.

737 Dessler, A. E., Z. Zhang, and P. Yang (2008), Water-vapor climate feedback inferred

738 from climate fluctuations, 2003-2008, Geophys. Res. Lett., 35, L20704, doi:

739 10.1029/2008GL035333.

740 Dessler, A. E. (2010), A determination of the cloud feedback from climate variations

741 over the past decade, Science, 330, 1523–1527, doi: 10.1126/ science.1192546.

742 Doelling, D. R., N. G. Loeb, D. F. Keyes, M. L. Nordeen, D. Morstad, C. Nguyen, B. A.

743 Wielicki, D. F. Young, and M. Sun, 2013: Geostationary enhanced temporal

744 interpolation for CERES flux products. J. Atmos. Oceanic Technol., 30, 1072-1090.

745   Harries J. E., J. E. Russell, J. A. Hanafin et al. (2005), The Geostationary Earth

746   Radiation Budget Project, **Bull. Of the American Meteo**. **Soc**. Vol: 86, ISSN: 0003-

747   0007.

748   Hartmann, D., and P. Ceppi (2013), Trends in the CERES Data set 2000-2013: The

749   effects of sea ice and jet shifts and comparison to climate models, J. Clim.,

750   doi:10.1175/JCLI-D-13-00411.1.

751   Hoyos, C. and P. J. Webster (2007), The role of intraseasonal oscillation on the

752   nature of monsoon precipitation, J. Clim., 20 (17), 4402-4424.

753   Huang, Y. and V. Ramaswamy (2009), Evolution and trend of the outgoing long-

754   wave radiation spectrum, J. Clim., 22, 4637–4651, doi:10.1175/2009JCLI2874.1.

755   Iacono, M., J. S. Delamere, E. J. Mlawer, M. W. Shephard, S. A. Clough, and W. D. Collins

756   (2008), Radiative forcing by long-lived greenhouse gases: Calculations with the AER

757   radiative transfer models, J. Geophys. Res., 113, D13103,

758   doi:10.2019/2008JD009944.

759   Jones,C., L.M.V. Carvalho, R.W. Higgins, D.E. Wallisor, and J.K.E. Schemm (2004),

760   Climatology of tropical intraseasonal convective anomalies: 1970-2002, J. Clim, 17,

761   523-539.

762   Kidson, J. W., M. J. Revell, B. Bhaskaran, A. B. Mullan, and J. A. Renwick (2002),

763   Convection patterns in the Tropical Pacific and their influence on the atmospheric

764   circulation at higher latitudes, J. Climate, 15, 137-159.

765   Kiladis, G. N., K. H. Straub, and P. T. Haertel (2005), Zonal and vertical structure of

766   the Madden-Julian Oscillation, J. Atmos. Sci., 62, 2790-2809.

767   Loeb, N. G., K. J. Priestley, D. P. Kratz, E. B. Geier, R. N. Green, B. A. Wielicki, P.O.R.

768   Hinton, S. K. Nolan (2001), Determination of unfiltered radiances from the clouds

769   and the earth's radiant energy system (CERES) instrument, J. Appl. Meteorol., 40,

770   822-835.

771   Loeb N. G., B. A. Wielicki, D. R. Doelling, G. L. Smith, D. F. Keyes, S. Kato, N. Manalo-

772   Smith, T. Wong (2009), Toward optimal closure of the Earth's top-of-atmosphere

773   radiation budget, J. Clim., 22, 748–766.

774   Loeb, N. G., J. M. Lyman, G. C. Johnson, R. P. Allan, D. R. Doelling, T. Wong, B. J. Soden,

775   and G. L. Stephens (2012), Observed changes in top-of-the-atmosphere radiation

776   and upper-ocean heating consistent within uncertainty, Nat. Geosci., 5,

777   doi:10.1038/NGEO1375.

778   Loeb, N. G., N. Manalo-Smith, W. Su, M. Shankar, and S. Thomas (2016), CERES top-

779   of-atmosphere Earth Radiation Budget Climate Data Record: accounting for in-orbit

780   changes in instrument calibration. Remote Sensing, 8(3), 182.

781   http://dx.doi.org/10.3390/rs8030182.

782   Loeb, N. G., D. R. Doelling, H.Wang , W. Su, C. Nguyen, J. G. Corbett, L. Liang, C.

783   Mitrescu, F. G. Rose, and S. Kato (2018), Clouds and the Earth's Radiant Energy

784   System (CERES) Energy Balanced and Filled (EBAF) Top-of-Atmosphere (TOA)

785   Edition-4.0 Data Product. J. Climate, 31, 895-918, doi: 10.1175/JCLI-D-17-0208.1.

786   Mehta, A. V. and J. Susskind (1999a), Outgoing longwave radiation from the TOVS

787   Pathfinder Path A Data Set, J. Geophys. Res., 104, 12193-12212.

788   Mehta, A. V. and J. Susskind (1999b), Longwave radiative flux calculations in the

789   TOVS Pathfinder Path A Data Set, NASA Tech. Rep., GSFC/CR-1999-208643.

790   Soden, B. J. and I. M. Held (2006), An assessment of climate feedbacks in coupled

791   ocean–atmosphere models, J. Clim., 19, 3354-3360.

792   Soden, B. J., I. M. Held, R. Colman, K. M. Shell, J. F. Kiehl, C. A. Shields (2008),

793   Quantifying climate feedbacks using radiative kernels, J. Clim., 21, 3504-3520.

794   Su, W. N.G.Loeb, L.Liang, N.Liu, and C. Liu (2017), The El Niño-Southern Oscillation

795   effect on tropical outgoing longwave radiation: A daytime versus nighttime perspective, J.

796   Geophys. Res. Atmos, 22, 7820–7833, doi: 10.1002/JD0270u 7820–7833.

797   Susskind, J., J. M. Blaisdell, L. Iredell, and F. Keita (2011), Improved temperature

798   sounding and quality control methodology using AIRS/AMSU Data: The AIRS

799   Science Team Version 5 retrieval algorithm. Geoscience and Remote Sensing, IEEE

800   Trans. on Geosci. and Remote Sens., Issue: 99, doi:10.1109/TGRS.2010.2070508, 1-

801   25.

802   Susskind, J., G. Molnar, L. Iredell, and N. G. Loeb (2012), Interannual variability of

803   outgoing longwave radiation as observed by AIRS and CERES, J. Geophys. Res., 117,

804   D23107, doi: 10.1029/2012JD017997.

805   Susskind, J., J. M. Blaisdell, and L. Iredell (2014), Improved methodology for surface

806   and atmospheric soundings, error estimates, and quality control procedures: the

807   atmospheric infrared sounder science team version-6 retrieval algorithm, J. Appl.

808   Rem. Sens., 8, 084994, doi:10.1117/1.JRS.8.084994.

809   Tian, B., D. E. Waliser, E. J. Fetzer, and Y. L. Yung (2010), Vertical moist

810   thermodynamic structure of the Madden-Julian oscillation in atmospheric infrared

811   sounder retrievals: An update and a comparison to ECMWF interim re-analysis,

812   Mon. Weather Rev., 138 (12), 4576-4582, ISSN 0027-0644.

813   Vonder Haar, T.H., J.L. Bytheway, and J.M. Forsythe (2012) Weather and climate

814   analyses using improved global water vapor observations, Geophys. Res. Lett., 39,

815   L15802, doi: 10.1029/20122GL052094.

816   Wong, T., B. A. Wielicki, R. B. Lee, III, G. L. Smith, K. A. Bush, J. K. Willis (2006),

817   Reexamination of the observed decadal variability of the Earth Radiation Budget

818   using altitude-corrected ERBE/ERBS nonscanner WFOV data, J. Clim., 19, 4028-4040.

819   Zelinka, M. D. and D. L. Hartmann (2011), The observed sensitivity of high clouds to

820   mean surface temperature anomalies in the tropics, J. Geophys. Res., 116, D23103,

821   doi: 10.1029/2011JD016459.

822   Zelinka, M. D., S. A. Klein, and D. L. Hartmann (2012a), Computing and partitioning

823   cloud feedbacks using cloud property histograms. Part 1: Cloud radiative kernels, J.

824   Clim., 25, 3715–3735, doi: 10.1175/JCLI-D- 11-00248.1.

825   Zelinka, M. D., S. A. Klein, and D. L. Hartmann (2012b), Computing and partitioning

826   cloud feedbacks using cloud property histograms. Part 2: Attribution to the nature

827   of cloud changes, J. Clim., 25, 3736–3754, doi:10.1175/JCLI-D-11-00249.1.

828

829   Table 1

830

	AIRS 1:30 AM minus CERES	AIRS 1:30 PM minus CERES	AIRS 1:30 AM/PM minus CERES
Global Mean			
Bias	-0.25	6.22	2.99
STD	0.22	0.38	0.25
Slope (W/m²/yr)	0.0018±0.0085	-0.0068± 0.0145	-0.0028±0.0094
Tropical Mean			
Bias	-0.21	7.62	3.71
STD	0.32	0.42	0.27
Slope (W/m²/yr)	0.0054±0.0122	-0.0080±0.0158	-0.0017±0.0102
30N-90N Mean			
Bias	-1.34	6.18	2.42
STD	0.73	1.15	0.37
Slope (W/m²/yr)	-0.0118±0.0277	-0.0022±0.0438	-0.0072±0.0142
30S-90S Mean			
Bias	-0.75	3.46	2.11
STD	0.90	0.45	0.33
Slope (W/m²/yr)	0.0082±0.0344	-0.0089±0.0171	-0.0007±0.0126

831

832

833 Table 2

	Global Mean	Tropical Mean	N. Hemisphere Extra-tropics	S. Hemisphere Extra-tropics
AIRS 1:30 PM	0.0024±0.0189	-0.0163±0.0361	0.0432±0.0406	-0.0008±0.0257
AIRS 1:30 AM	0.0110±0.0163	-0.0029±0.0312	0.0510±0.0343	-0.0012±0.0261
AIRS 1:30 AM/PM	0.0064±0.0174	-0.0100±0.0335	0.0469±0.0370	-0.0013±0.0256
CERES	0.0112±0.0179	-0.0063±0.0345	0.0554±0.0366	0.0020±0.0259

834

835

Table A1

Band Number	Frequency Range	Clear Sky OLR		OLR		LWCRF	
		Flux	%	Flux	%	Flux	%
1	100-350	34.79	13.03	34.40	14.14	0.39	1.65
2	350-500	42.90	16.06	40.97	16.84	1.93	8.09
3	500-630	38.94	14.58	36.46	14.99	2.48	10.41
4	630-700	10.27	3.85	10.26	4.22	0.01	0.06
5	700-820	32.37	12.12	29.04	11.94	3.33	13.96
6	820-980	46.77	17.51	39.89	16.40	6.88	28.83
7	980-1080	16.88	6.32	14.50	5.96	2.37	9.96
8	1080-1180	17.69	6.62	14.73	6.05	2.97	12.44
9	1180-1390	17.13	6.41	14.70	6.04	2.43	10.20
10	1390-1480	2.43	0.91	2.26	0.93	0.17	0.72
11	1480-1800	2.95	1.10	2.78	1.14	0.17	0.70
12	1800-2080	2.37	0.89	2.01	0.83	0.36	1.53
13	2080-2250	0.79	0.30	0.63	0.26	0.16	0.69
14	2250-2380	0.05	0.02	0.05	0.02	0.00	0.00
15	2380-2600	0.44	0.16	0.34	0.14	0.10	0.44
16	2600-3260	0.34	0.13	0.25	0.10	0.08	0.34

Figure and Table Captions

841

842   Table 1:

843   Area mean values of the mean difference (AIRS OLR minus CERES OLR), and
844   standard deviation (STD) of the differences, for each of the three sets of AIRS OLR,
845   as well as the slopes of the linear least squares fit to the differences between AIRS
846   and CERES OLR (W/m^2/yr) for the period September 2002 through August 2016. The
847   uncertainties of the slopes are twice the STDs of the linear least squares fits to the time
848   series of differences.

849

850   Table 2:

851   Area mean AIRS and CERES OLR ARCs (W/m^2/yr). The uncertainties of the ARCs are
852   twice the STDs of the linear least squares fits to the anomaly time series.

853

854

855

856   Table A1:

857   Frequency ranges of the spectral bands used to compute AIRS OLR global mean
858   annual mean band fluxes (W/m^2), and the percentage contribution of each band to
859   Clear Sky OLR, OLR, and LWCRF.

860

861   Figure 1

862   Monthly mean area mean AIRS and CERES OLR time series data from September
863   2002 through August 2016 over four spatial domains: global; the Northern
864   Hemisphere extra-tropics; the tropics; and Southern Hemisphere extra-tropics. The
865   vertical black lines indicate January of each year.

866

867   Figure 2

868   The differences (AIRS minus CERES) of area mean OLR time series from September
869   2002 through August 2016 over the same four spatial domains shown in Figure 1.

870

871   Figure 3

872   AIRS and CERES monthly mean January OLR climatologies and climatological
873   differences on a 1°x1° spatial scale. The statistics under each figure indicate the area
874   weighted global mean (GM) value of the field and the area weighted spatial standard
875   deviation (STD).

876

877   Figure 4

878   AIRS and CERES monthly mean July OLR climatologies and climatological
879   differences on a 1°x1° spatial scale.

880

881   Figure 5

882   AIRS day minus night climatological differences of Surface Skin Temperature,
883   Radiative Effective Cloud Fraction, and 500 mb Specific Humidity for January and
884   July.

885

886   Figure 6

887   AIRS and CERES monthly mean area mean OLR anomaly time series from
888   September 2002 through August 2016 over four spatial domains: global; the
889   Northern Hemisphere extra-tropics; the tropics; and the Southern Hemisphere
890   extra-tropics. The tropical OLR anomaly time-series also shows monthly mean
891   values of the El Niño Index.

892

893   Figure 7

894   ARCs (W/m^2/yr) and ENCs of AIRS$_{AVG}$ OLR and CERES OLR over the time-period
895   September 2002 through August 2016. The NOAA Niño-4 region is outlined in black,
896   and the NOAA Niño-3 region is outlined in gray, in this figure as well as in some
897   subsequent figures.

898

899   Figure 8

900   Spatial 1° latitude by 1° longitude distributions of ARCs of AIRS$_{AVG}$ Surface Skin
901   Temperature, Surface Air Temperature, 500 mb Specific Humidity, and Radiative
902   Effective Cloud Fraction over the time period September 2002 through August 2016.

903

904

905   Figure 9

906   Spatial 1° latitude by 1° longitude distributions of ENCs of AIRS$_{AVG}$ Surface Skin
907   Temperature, Surface Air Temperature, 500 mb Specific Humidity, and Radiative
908   Effective Cloud Fraction over the time-period September 2002 through August 2016.

909

910   Figure 10

911   Hovmöller diagrams of AIRS$_{AVG}$ monthly mean anomaly time-series integrated over
912   the latitude range 5°N through 5°S (vertical scale) in each 1° longitude bin
913   (horizontal scale), for the period September 2002 through August 2016. a) Surface
914   Skin Temperature (K), b) OLR (W/m^2), c) 500 mb Specific Humidity (g/kg), d)
915   Radiative Effective Cloud Fraction (%).

916

917   Figure 11

918   ARCs over the time-period September 2002 through August 2016 of AIRS 1:30 PM
919   Surface Skin Temperature, AIRS 1:30 AM Surface Skin Temperature, AIRS 1:30 PM
920   minus 1:30 AM Surface Skin Temperature, and AIRS 1:30 PM minus 1:30AM 500 mb
921   Specific Humidity.

922

923   Figure 12

924   ENCs over the time-period September 2002 through August 2016 of AIRS 1:30 PM
925   Surface Skin Temperature, AIRS 1:30 AM Surface Skin Temperature, AIRS 1:30 PM
926   minus 1:30 AM Surface Skin Temperature, and AIRS 1:30 PM minus 1:30 AM 500
927   mb Specific Humidity.

928

929   Figure 13

930   Monthly mean Surface Skin Temperature anomaly time series averaged over
931   Eastern Australia for the time period September 2002 through August 2016 a)1:30
932   PM, b)1:30 AM, and c)1:30 PM minus 1:30 AM. Also shown on each figure is twice
933   the ENI.

934

Figure 1.

Area Mean OLR Time Series (W/m^2)
September 2002 through August 2016
Global

30°N to 30°S

30°N to 90°N

30°S to 90°S

AIRS 1:30 PM   AIRS 1:30 AM   AIRS AM/PM Average   CERES

Figure 2.

Area Mean OLR Time Series Differences from CERES (W/m^2)
September 2002 through March 2016

Global
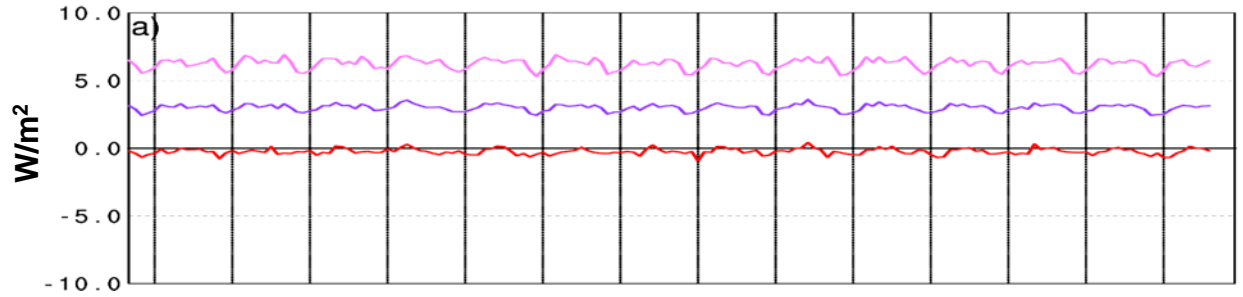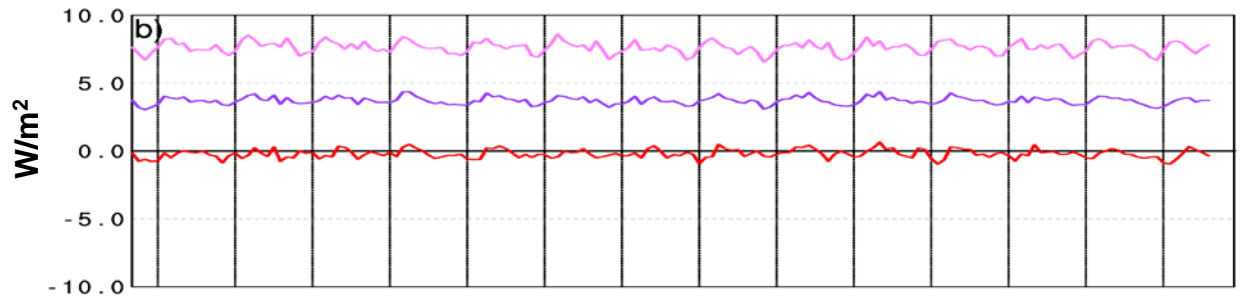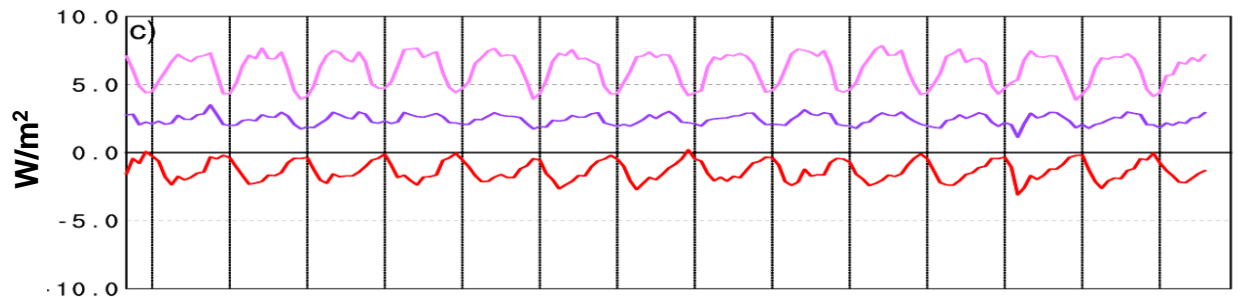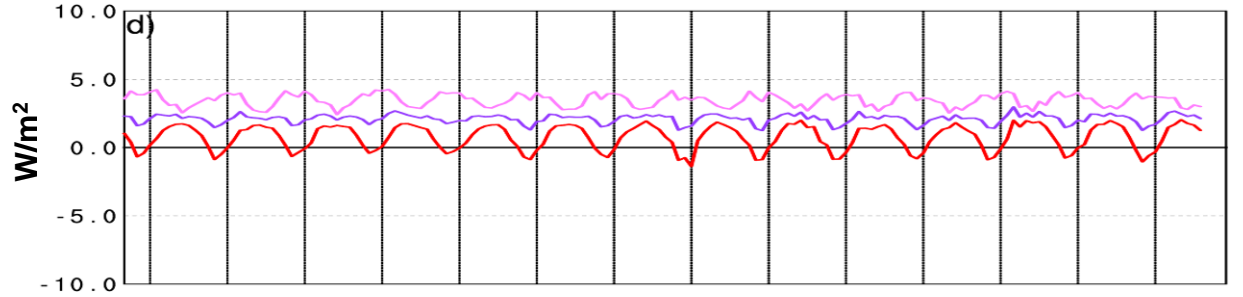
a)

30°N to 30°S

b)

30°N to 90°N

c)

30°S to 90°S

d)

AIRS 1:30 PM   AIRS 1:30 AM   AIRS AM/PM Average

Figure 3.

Outgoing Longwave Radiation (W/m^2)
January Climatology

a) AIRS 1:30 AM/PM Average
b) CERES
c) AIRS 1:30 AM/PM minus CERES

Mean= 240.15 STD= 31.66
Mean= 237.45 STD= 31.55
GM= 2.71 STD= 2.58

d) AIRS 1:30 AM minus CERES
e) AIRS 1:30 PM minus CERES
f) AIRS 1:30 PM minus 1:30 AM

GM= -0.38 STD= 4.19
GM= 5.80 STD= 7.48
GM= 6.19 STD=10.97
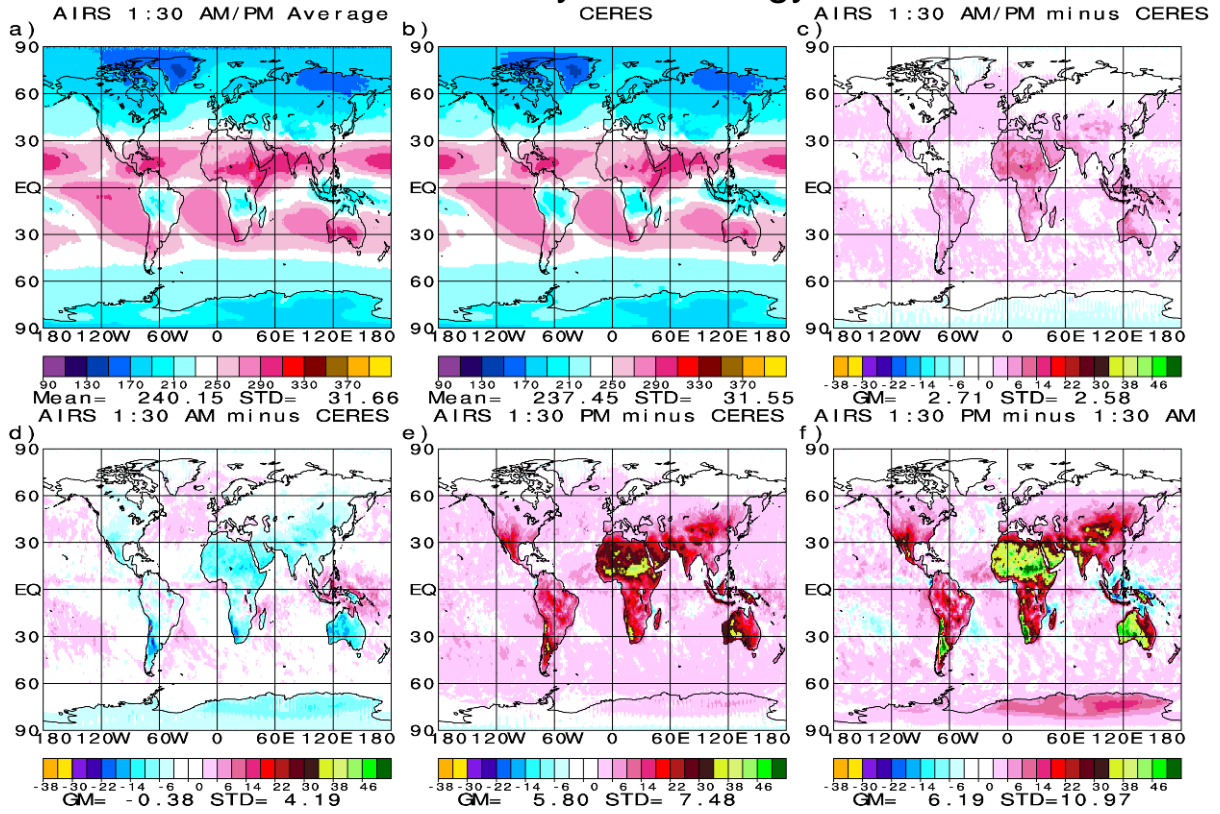
Figure 4.

Outgoing Longwave Radiation (W/m^2)
July Climatology

a) AIRS 1:30 AM/PM Average

b) CERES

c) AIRS 1:30 AM/PM minus CERES

Mean= 247.44 STD= 32.83

Mean= 244.32 STD= 32.60

GM= 3.12 STD= 2.67

d) AIRS 1:30 AM minus CERES

e) AIRS 1:30 PM minus CERES

f) AIRS 1:30 PM minus 1:30 AM

GM= -0.02 STD= 5.13

GM= 6.26 STD= 8.57

GM= 6.29 STD=13.07
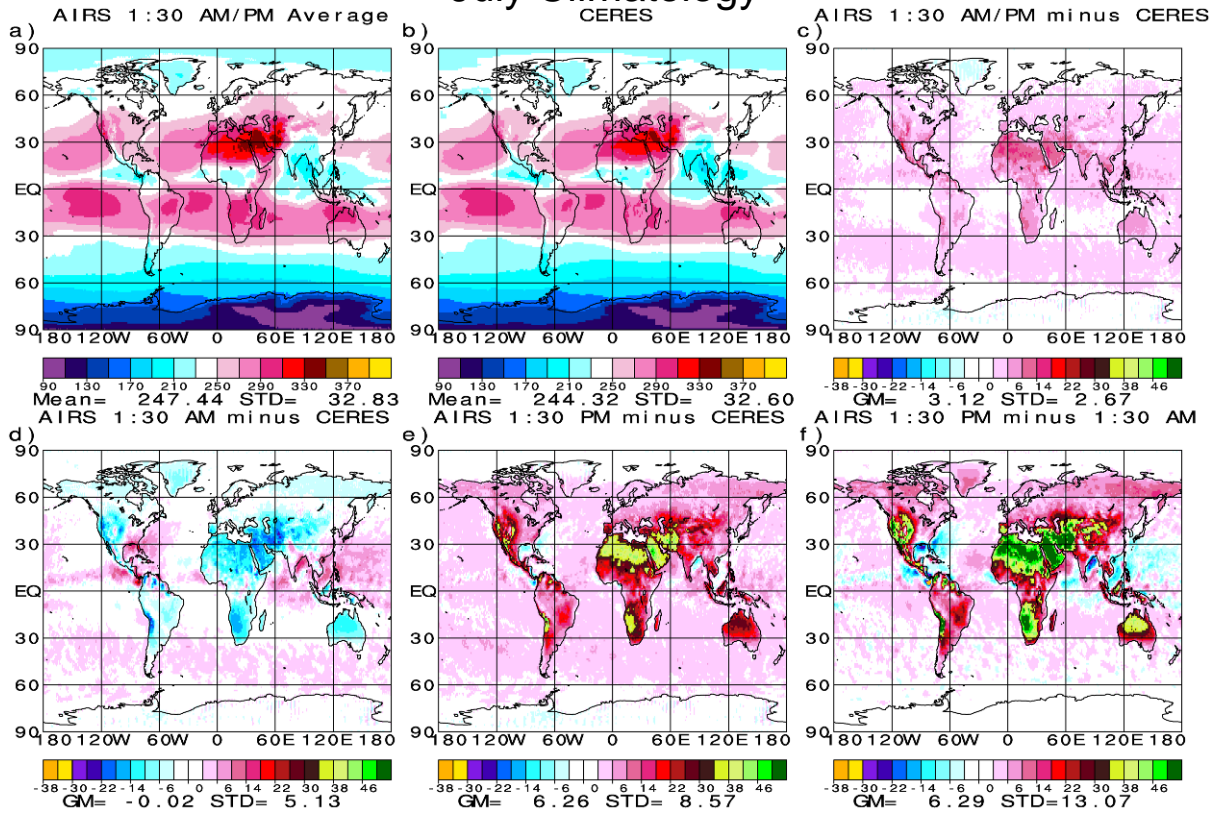
Figure 5.

1:30 PM minus 1:30 AM Climatological Differences

a) January
Surface Skin Temp (K)
-46 -38 -30 -22 -14 -6 0 4 10 18 26 34
GM= 4.03 STD= 7.36

b) January
Cloud Fraction (%)
-46 -38 -30 -22 -14 -6 0 6 14 22 30 38
Mean= -5.38 STD= 7.23

c) January
500 mb Sp Hum (g/kg)
-0.92 -0.60 -0.28 0.00 0.28 0.60
GM= 0.02 STD= 0.07

d) July
Surface Skin Temp (K)
-46 -38 -30 -22 -14 -6 0 4 10 18 26 34
GM= 4.73 STD= 8.39

e) July
Cloud Fraction (%)
-46 -38 -30 -22 -14 -6 0 6 14 22 30 38
Mean= -4.99 STD= 8.70

f) July
500 mb Sp Hum (g/kg)
-0.92 -0.60 -0.28 0.00 0.28 0.60
GM= 0.03 STD= 0.08

Figure 6.

Area Mean OLR Time Series Anomaly (W/m²/yr)
September 2002 through August 2016

Global

30°N to 30°S

30°N to 90°N

30°S to 90°S

AIRS 1:30 PM   AIRS 1:30 AM   AIRS AM/PM Average   CERES

El Niño Index
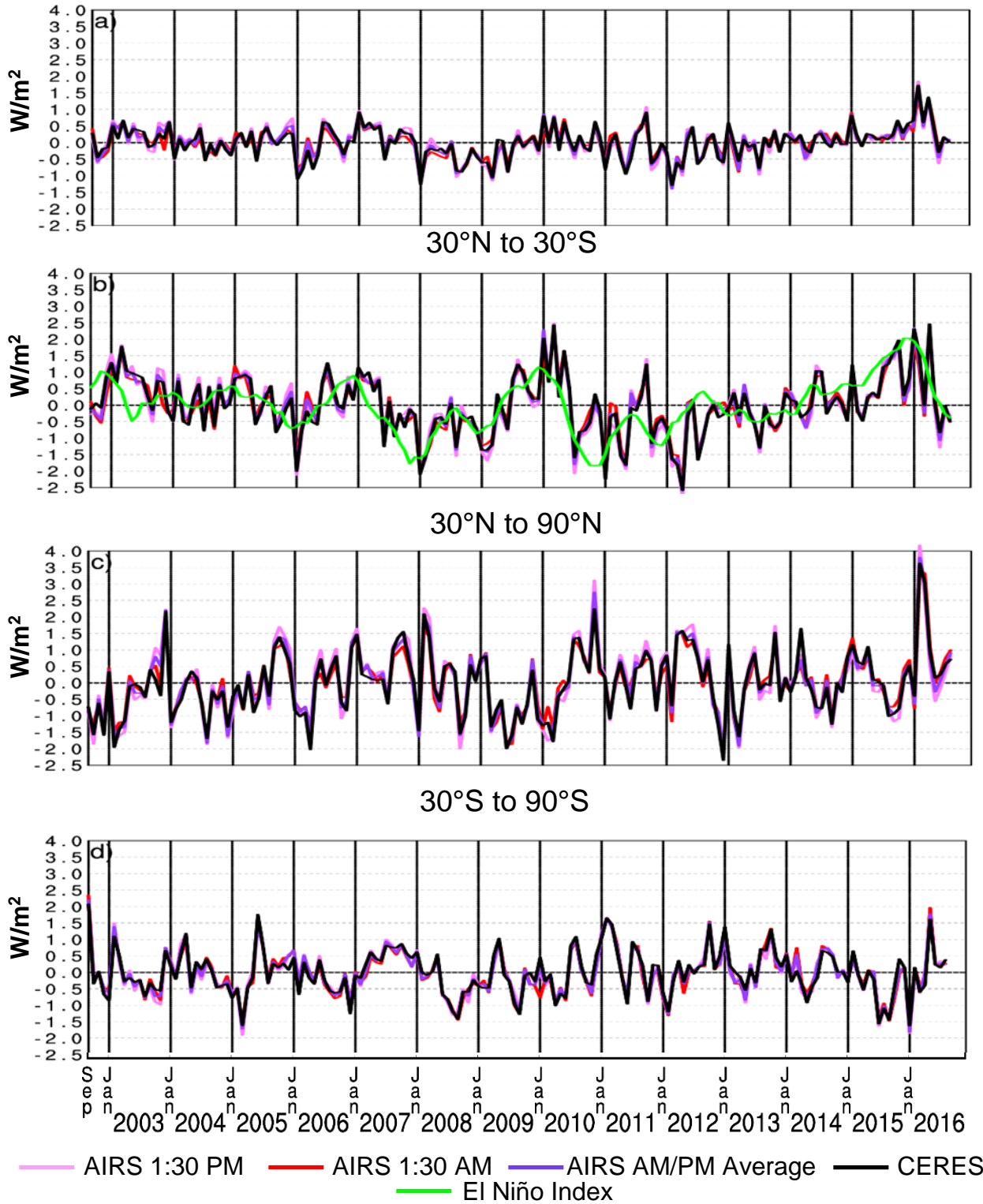
Figure 7.

OLR ARC's (W/m²/yr) September 2002 through August 2016

a) AIRS Average

b) CERES

Mean = 0.006 STD = 0.222

Mean = 0.011 STD = 0.227

c) AIRS Average minus CERES

d) AIRS 1:30 PM minus 1:30 AM

Mean = -0.005 STD = 0.047 Cor= 0.978

Mean = -0.009 STD = 0.116 Cor= 0.871

OLR ENC's September 2002 through August 2016

e) AIRS Average

f) CERES

Mean = 0.010 STD = 0.222

Mean = 0.013 STD = 0.243
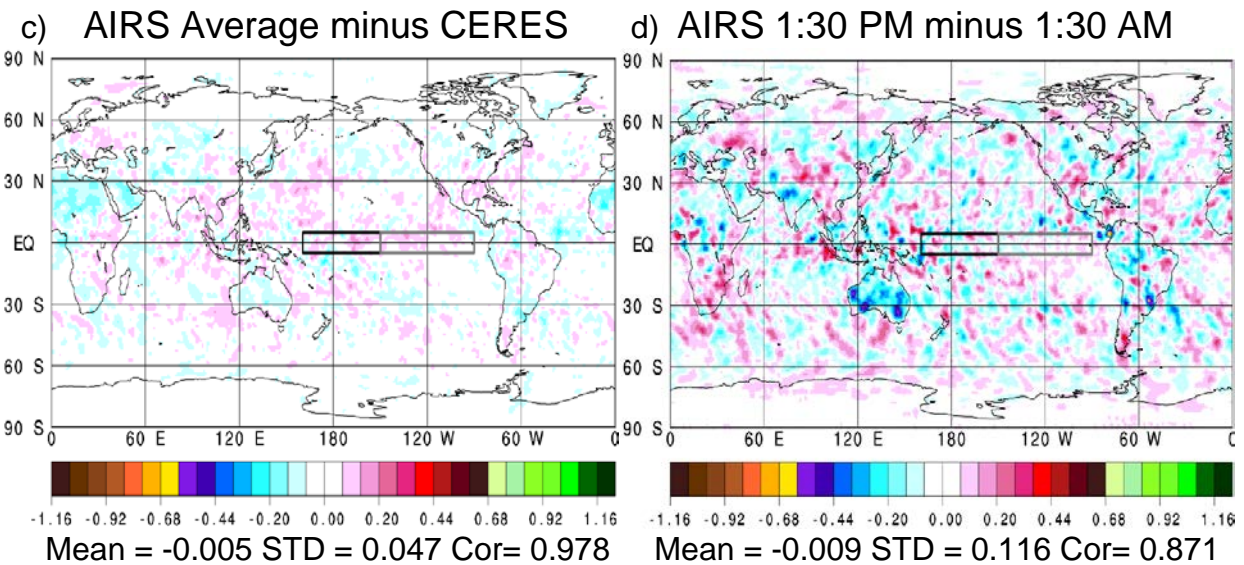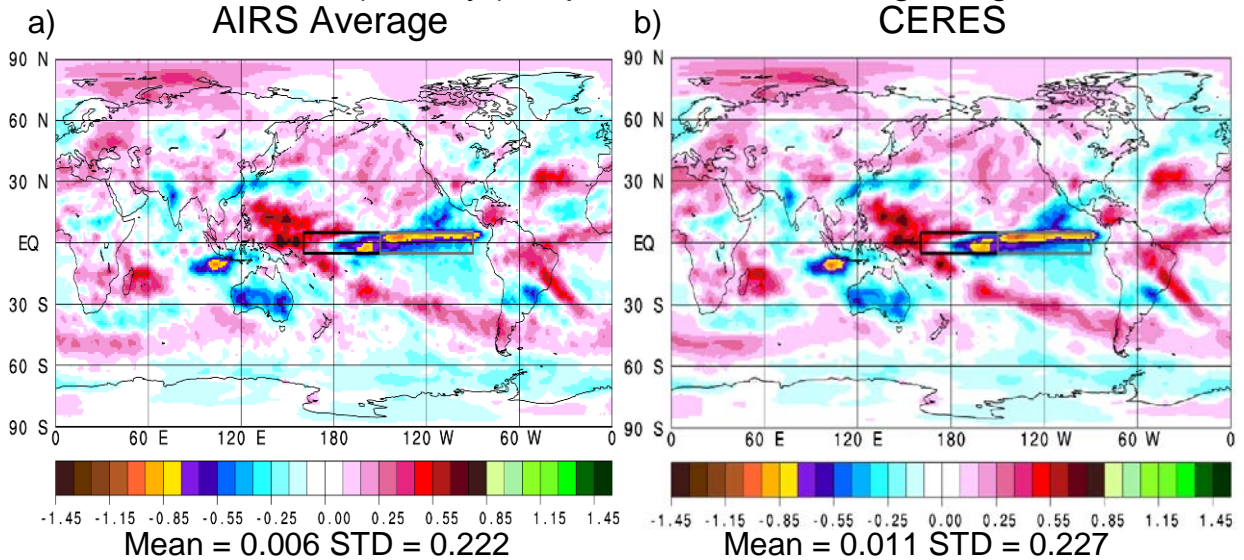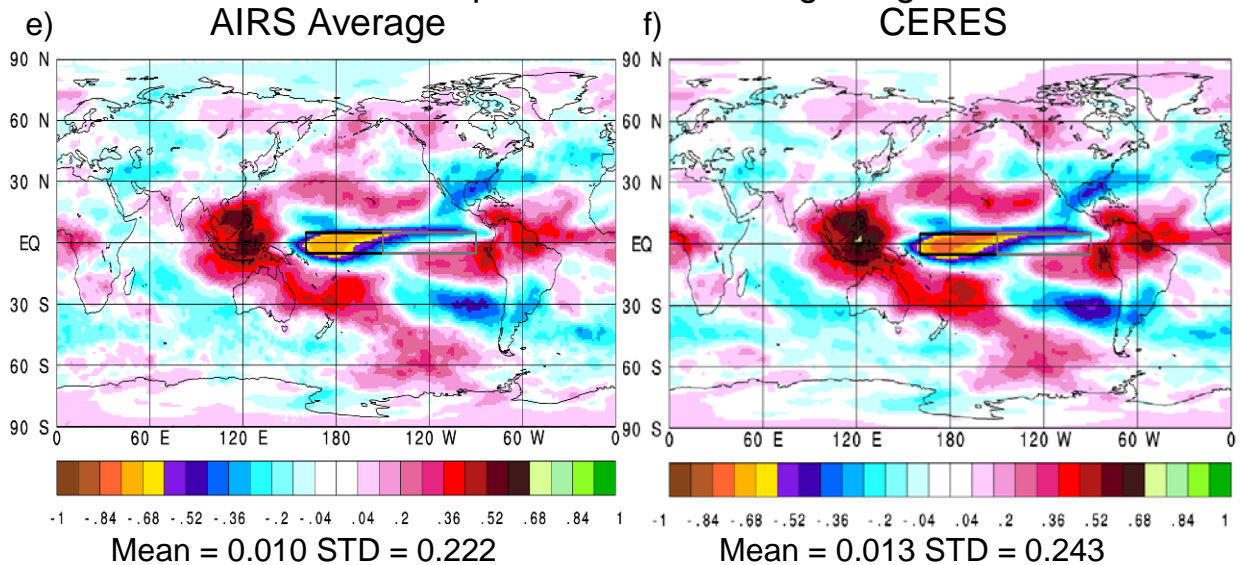
Figure 8.

AIRS Average ARC's September 2002 through August 2016

a) Surface Skin Temperature (K/yr)

Mean = 0.019 STD = 0.036

b) Surface Air Temperature (K/yr)

Mean = 0.016 STD = 0.029

c) 500 mb Specific Humidity (g/kg/yr)

Mean = 0.066 STD = 0.709
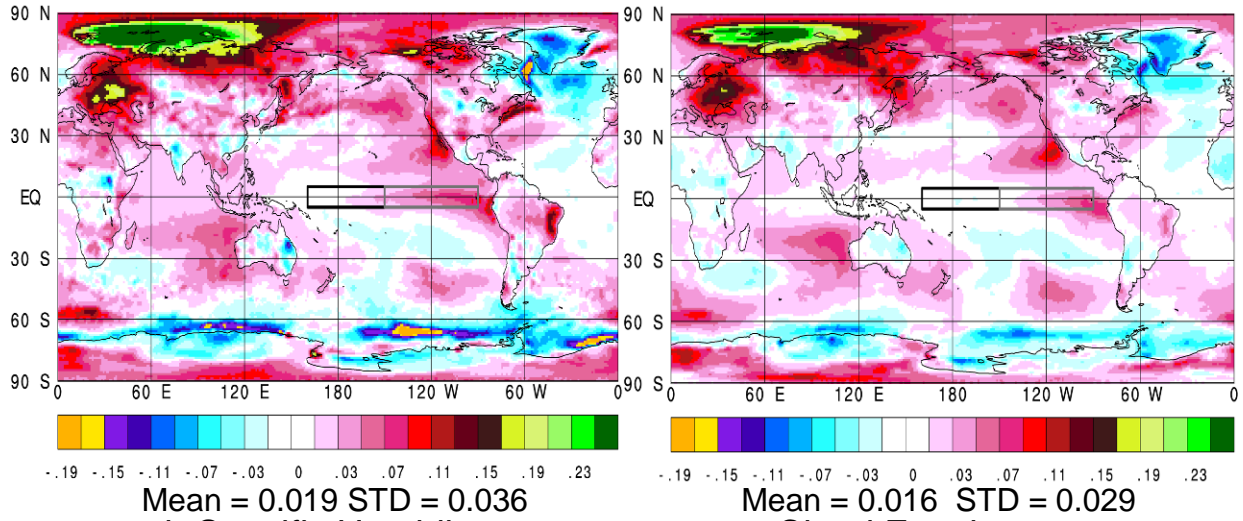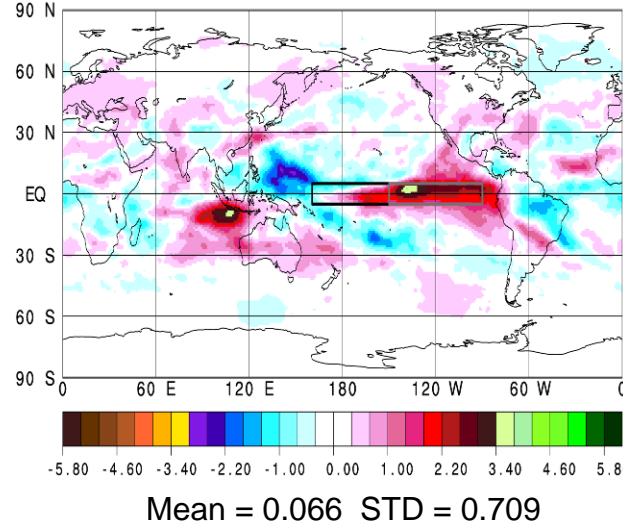
d) Cloud Fraction (%/yr)

Mean = 0.023 STD = 0.161
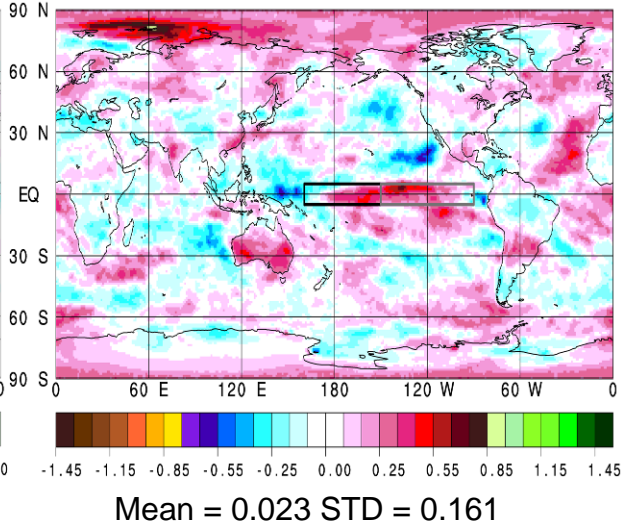
Figure 9.

AIRS Average ENC's September 2002 through August 2016

a) Surface Skin Temperature

b) Surface Air Temperature

Mean = 0.08 STD = 0.28

Mean = 0.07 STD = 0.25

c) 500 mb Specific Humidity

d) Cloud Fraction

Mean = 0.02 STD = 0.22

Mean = -0.02 STD = 0.18
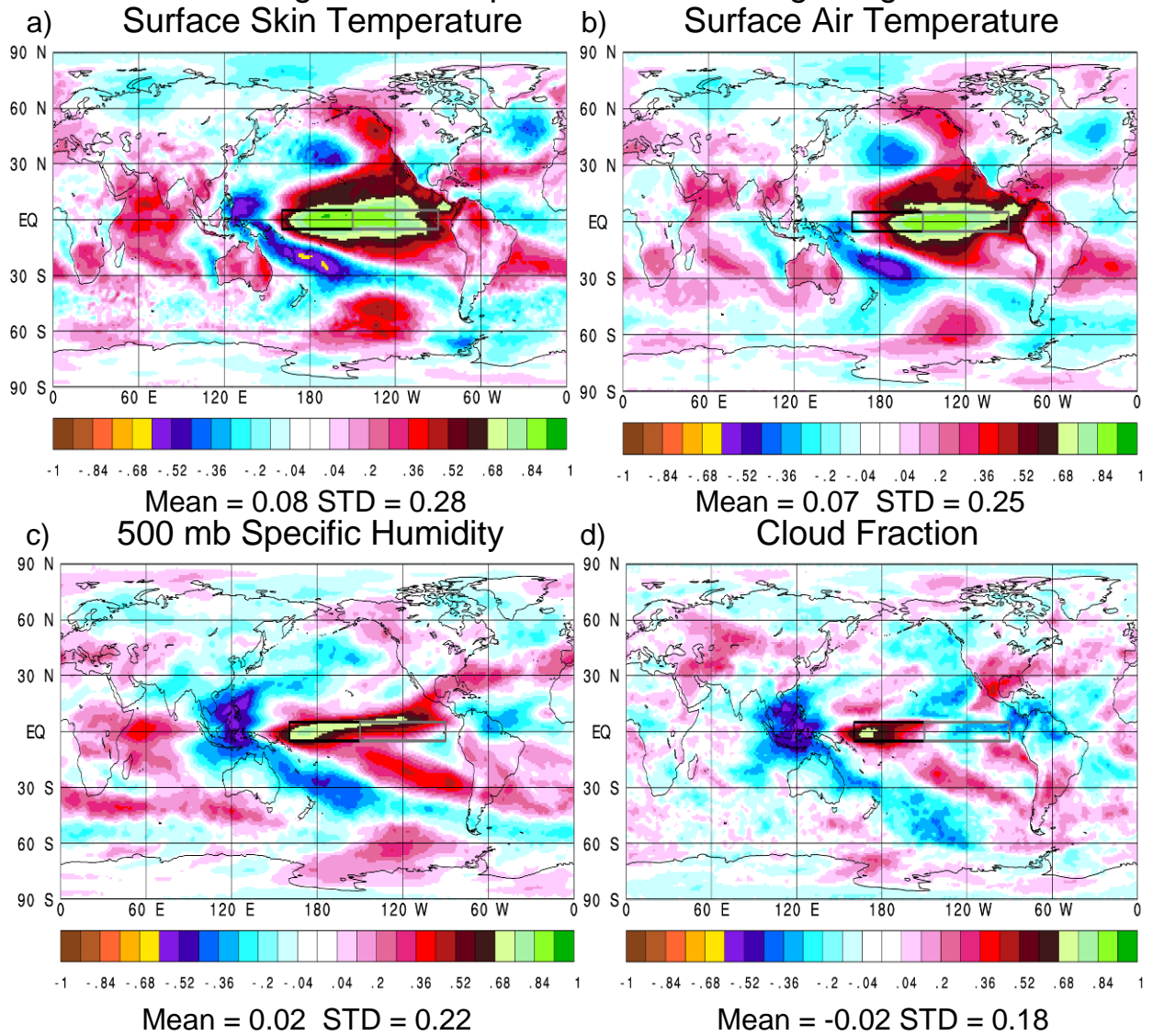
Figure 10.

AIRS Anomalies Tropics 5°N to 5°S September 2002 through August 2016

a) Surface Skin Temperature (K)
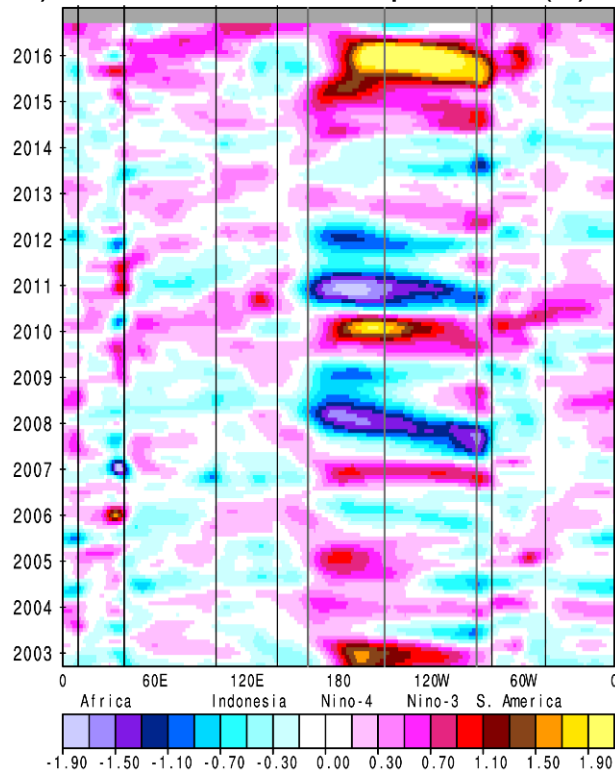
b) OLR (W/m²)
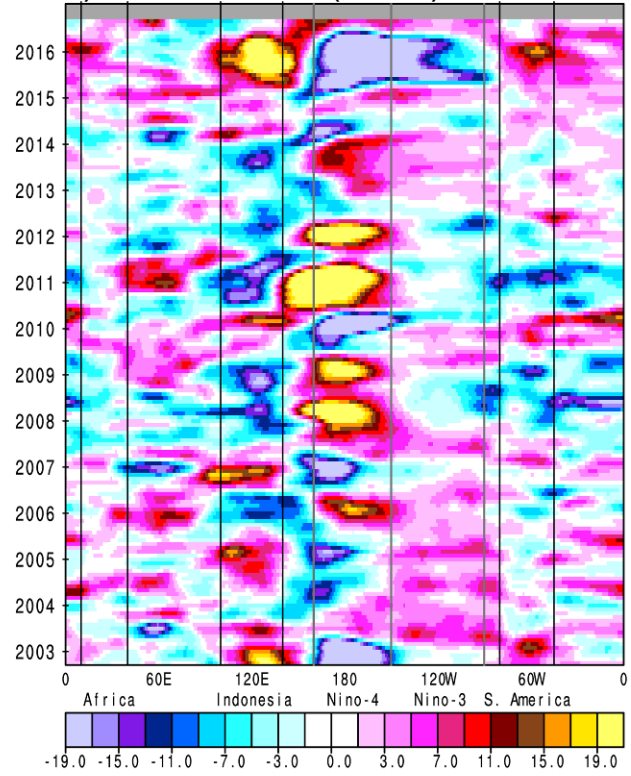
c) 500 mb Specific Humidity (g/kg)
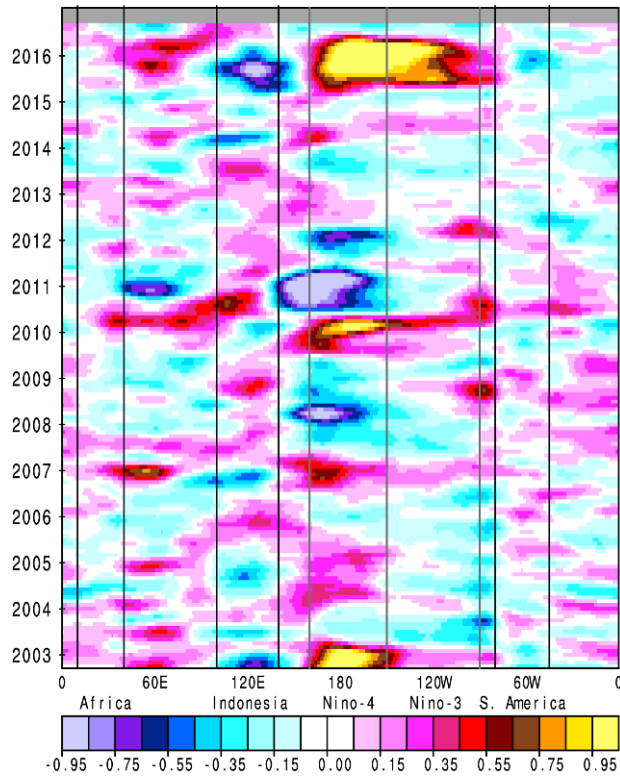
d) Cloud Fraction (%)
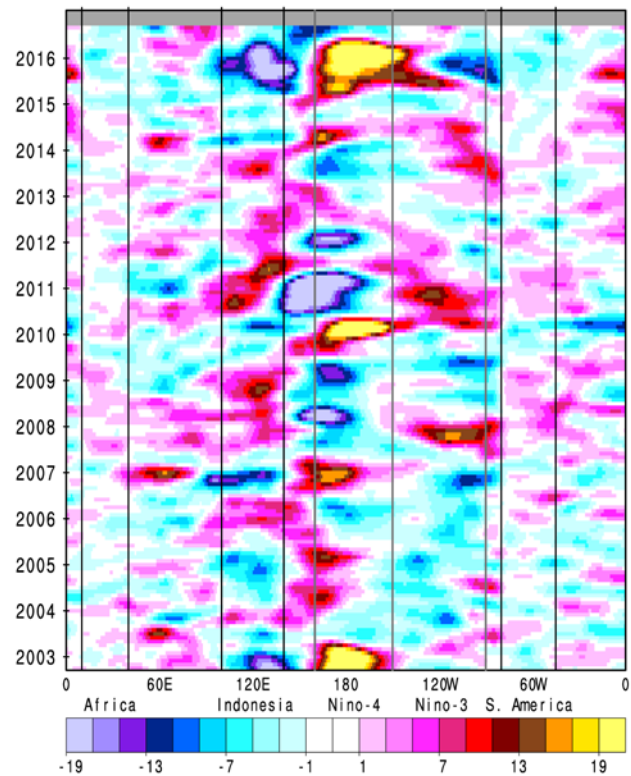
Figure 11.

AIRS ARC's September 2002 through August 2016

a) Surface Skin Temperature (K/yr) 1:30 PM

b) Surface Skin Temperature (K/yr) 1:30 AM
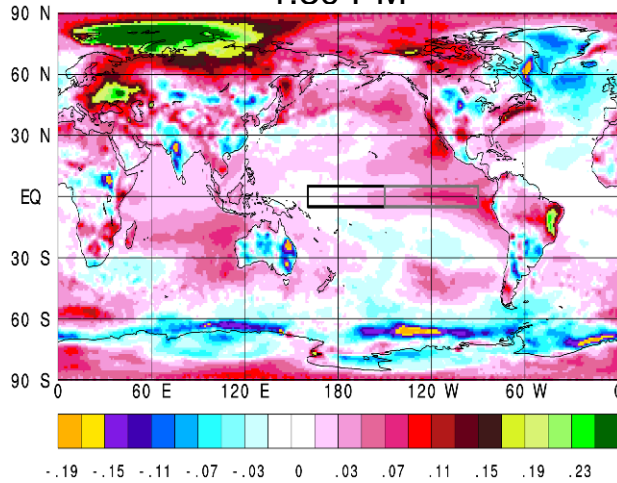
Mean = 0.019 STD = 0.041
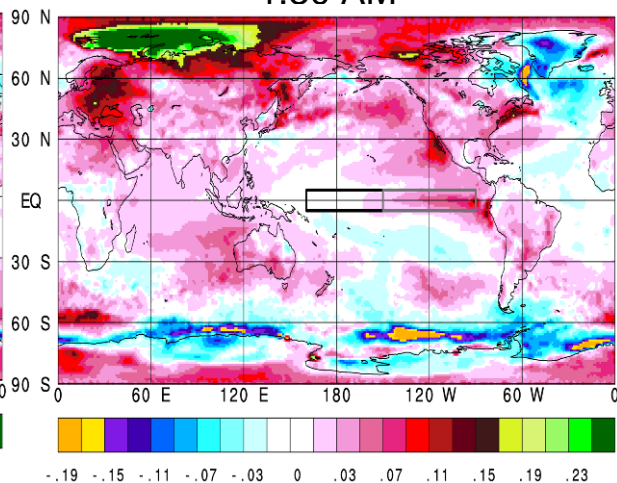
Mean = 0.019 STD = 0.035

c) Surface Skin Temperature (K/yr) PM minus AM
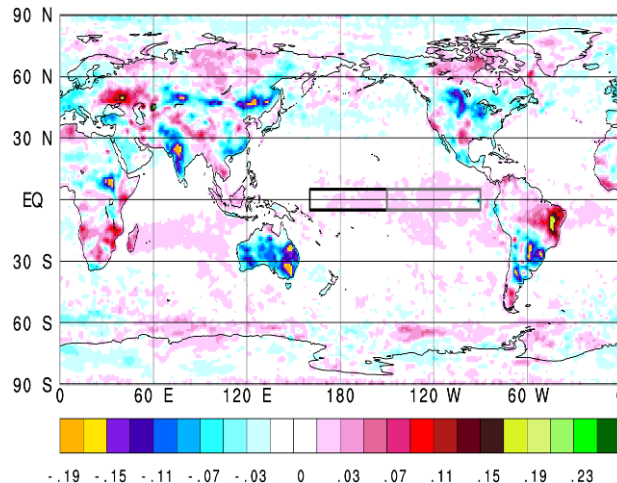
d) 500 mb Specific Humidity (g/kg/yr) PM minus AM
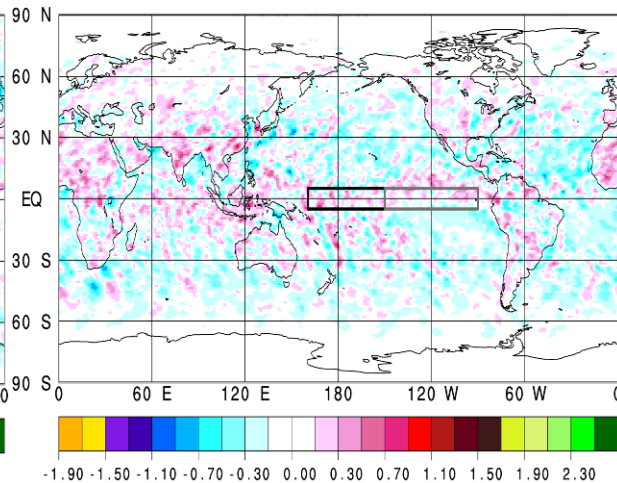
Mean = 0.000 STD = 0.027

Mean = -0.053 STD = 0.209

Figure 12.

AIRS ENC's September 2002 through August 2016

a) Surface Skin Temperature
1:30 PM
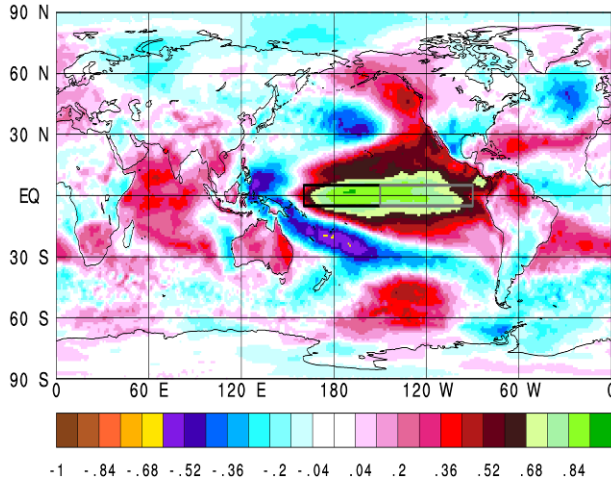
Mean = 0.08 STD = 0.28

b) Surface Skin Temperature
1:30 AM
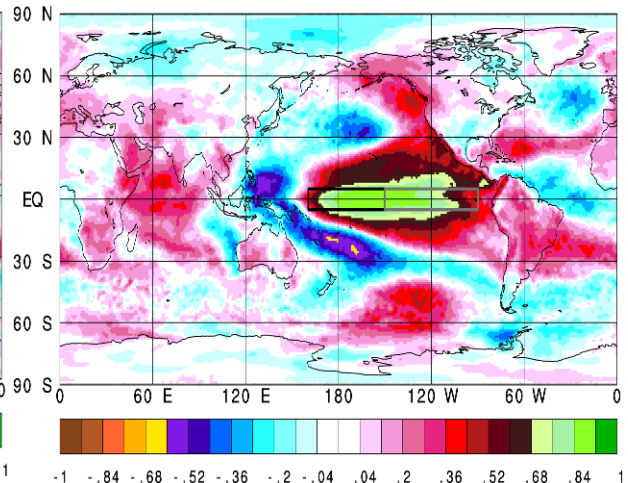
Mean = 0.08 STD = 0.028

c) Surface Skin Temperature
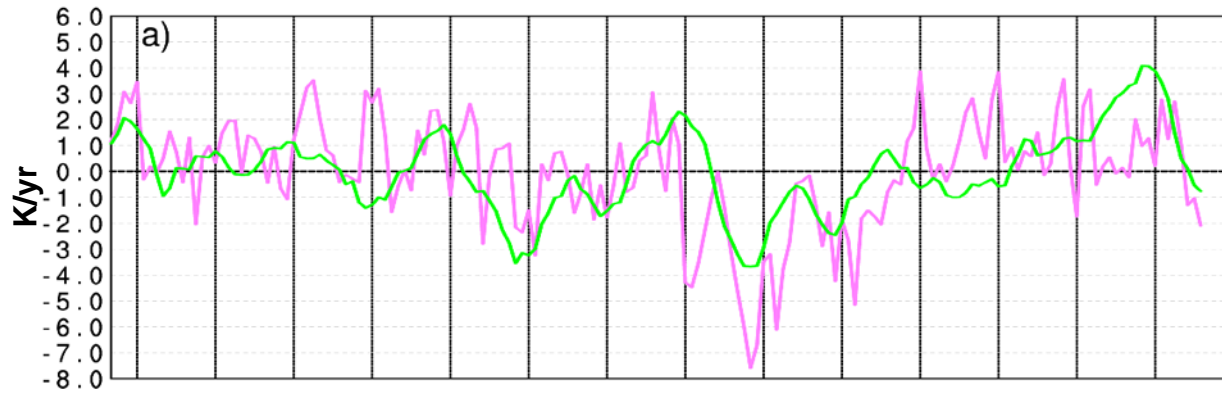PM minus AM
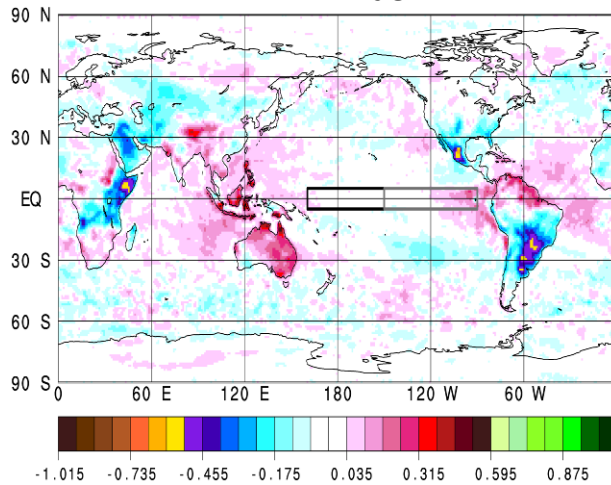
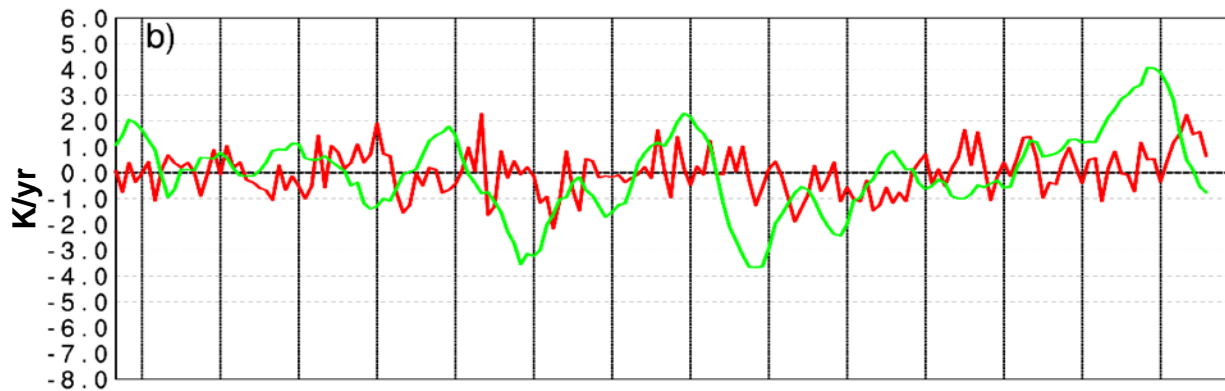Mean = 0.00 STD = 0.01

d) 500 mb Specific Humidity
PM minus AM
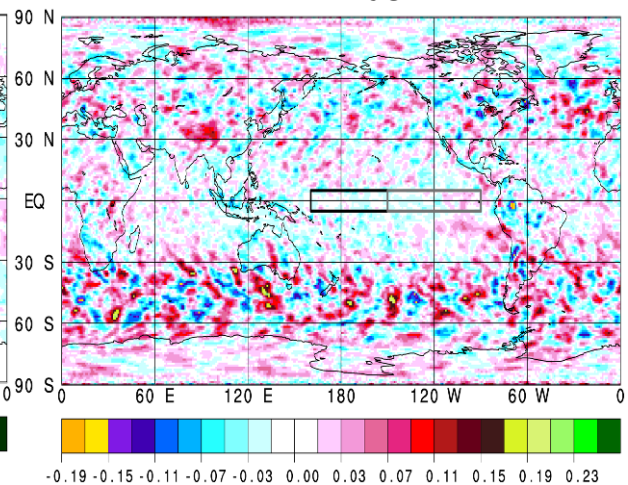
Mean = 0.00 STD = 0.04
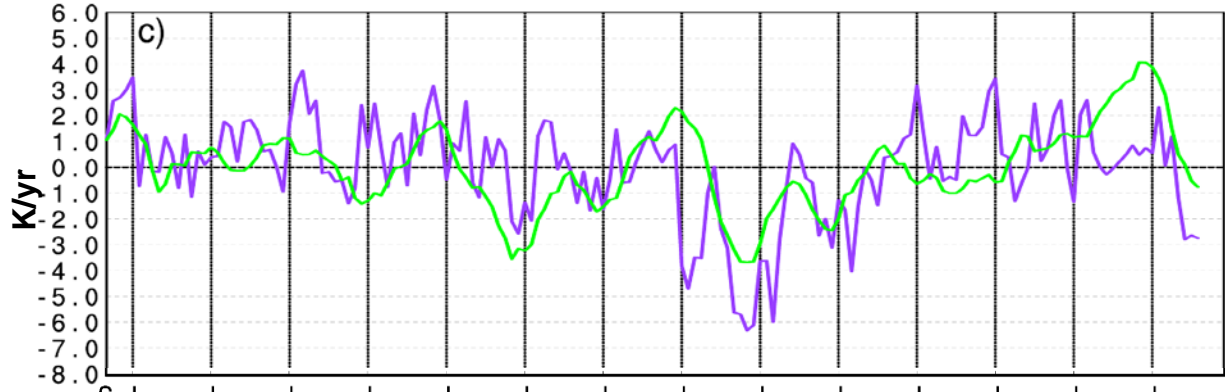
Figure 13.

Surface Skin Temperature Time Series Anomaly (K/yr)
Eastern Australia September 2002 through August 2016